

Master`s Thesis

Synthesis and Characterization of Mass and Charge Transport
Properties of the New Rare Earth Nickelate $\text{Pr}_2\text{Ni}_{0.9}\text{Co}_{0.1}\text{O}_{4+\delta}$

Author

Anna Theresa Strasser

Supervisor

assoc. Prof. Dipl.-Ing. Dr.mont. Edith Bucher

Montanuniversitaet Leoben, Chair of Physical Chemistry



August 2017

Acknowledgements

I would like to thank all the people who contributed in some way to the work described in my master thesis. First of all, I want to express my gratitude to my supervisor Edith Bucher who has supported me throughout my thesis with patience and knowledge. One simply could not wish for a better or friendlier supervisor!

Furthermore I would like to thank Professor Werner Sitte, Andreas Egger, Johannes Hofer, Nina Schroedl and Christian Berger for introducing me to the topic, for useful comments, remarks and engagement through my master thesis.

I would like to thank my loved one Andreas and my family. They have supported me throughout my whole academic studies. I will be grateful forever for their support and love!

Finally, this research was supported by the Austrian Research Promotion Agency FFG (Project No. 853538). Financial support by the “Klima- und Energiefonds” within the program “Energieforschung (E!MISSION)” is gratefully acknowledged.

Eidesstattliche Erklärung

Ich erkläre an Eides statt, dass ich die vorliegende Arbeit selbstständig verfasst, andere als die angegebenen Quellen/Hilfsmittel nicht benutzt, und die den benutzten Quellen wörtlich und inhaltlich entnommenen Stellen als solche kenntlich gemacht habe.

Statutory Declaration

I declare that I have authored this thesis independently, that I have not used other than the declared sources/resources, and that I have explicitly marked all material which has been quoted either literally or by content from the used sources.

Datum / Date

Unterschrift / Signature

If the challenge exists so must the solution!

Rona Mlnarik

Table of Contents

1. Theory.....	10
1.1. Rare Earth Nickelates.....	10
1.1.1. Crystal Structure.....	10
1.1.2. Diffusion Mechanism.....	13
1.1.3. Diffusion in Oxygen-Deficient Materials	16
1.2. Properties of Praseodymium Nickel Oxide	18
1.3. Freeze Drying	19
1.4. Four Point dc-van der Pauw Technique.....	21
1.4.1. Electrical Conductivity Measurement	23
1.4.2. Conductivity Relaxation Measurement.....	24
1.5. X-Ray Diffraction	28
1.6. Thermal Analysis	30
1.6.1. Dilatometry Analysis (Thermal Expansion Coefficient).....	30
1.6.2. Thermogravimetric Analysis.....	32
1.6.3. Differential Scanning Calorimetry	34
2. Synthesis and Preparation of a Dense PNCO Sample	35
2.1. Material Synthesis	36
2.2. Milling Process.....	39
2.3. Sample Preparation According to van der Pauw	40
3. Characterization	43
3.1. Crystal Structure and Phase Composition	43
3.2. Optimization of Sintering Program.....	45
3.3. Thermal Expansion Coefficient (TEC)	48
3.4. Thermogravimetric Analysis.....	50
3.5. Differential Scanning Calorimetry	53

3.6. Mass and Charge Transport Properties	57
3.6.1. Experimental Setup	57
3.6.2. Electronic Conductivity Measurement (σ)	59
3.6.3. Chemical Surface Exchange Coefficient (k_{chem}).....	62
3.7. Surface Analysis	66
4. Summary and Conclusion	70

Abstract

The focus of the present study is on the synthesis and characterization of the novel K_2NiF_4 -type oxide $Pr_2Ni_{0.9}Co_{0.1}O_{4+\delta}$ (PNCO). Ni in $Pr_2NiO_{4+\delta}$ is partially substituted with Co in order to increase the surface exchange coefficient of oxygen. The crystal structure, as well as mass and charge transport properties, especially oxygen exchange kinetics, of PNCO are studied. PNCO shows promising properties for application in air electrodes of solid oxide fuel cells or electrolyzer cells, electrochemical sensors, oxygen permeable membranes etc.

To obtain higher quantities of chemically homogeneous, single phase $Pr_2Ni_{0.9}Co_{0.1}O_{4+\delta}$ powder in one batch, a new freeze drying method based on aqueous acetate precursor solutions was developed. The solutions were mixed, shock-frozen in liquid nitrogen, and freeze-dried. During calcination the complex oxide was formed. X-ray powder diffraction (XRD) and Rietveld refinement verified that the material was single phase, and confirmed the K_2NiF_4 structure. The $Pr_2Ni_{0.9}Co_{0.1}O_{4+\delta}$ powder was further characterized by dilatometry, differential scanning calorimetry (DSC) and thermogravimetric analysis (TG). In pure Ar, a transition from the orthorhombic to the tetragonal K_2NiF_4 modification occurred, which was also reported for $Pr_2NiO_{4+\delta}$ [1-3]. Based on the dilatometry curve a pellet was sintered at 1120°C to obtain a dense sample for oxygen exchange measurements. However, XRD of the sintered pellet, as well as DSC and TG of powder samples, indicated that phase decomposition of $Pr_2Ni_{0.9}Co_{0.1}O_{4+\delta}$ into $Pr_4(Ni,Co)_3O_{10-x}$ and Pr-oxide occurs at $T \geq 750^\circ C$ and $pO_2 = 0.2$ bar as previously reported also for $Pr_2NiO_{4+\delta}$ [1-3]. Finally, by optimization of the sintering program, it was possible to obtain a phase-pure $Pr_2Ni_{0.9}Co_{0.1}O_{4+\delta}$ pellet with 97% of the theoretical density, which was used for studies of the oxygen exchange kinetics by the dc-conductivity relaxation method. In addition to that, a $Pr_2NiO_{4+\delta}$ pellet was prepared as a reference sample. For all three specimens (phase decomposed $Pr_2Ni_{0.9}Co_{0.1}O_{4+\delta}$, phase pure $Pr_2Ni_{0.9}Co_{0.1}O_{4+\delta}$, and Co-free reference $Pr_2NiO_{4+\delta}$) the electronic conductivity and the surface exchange coefficient were determined and compared with each other in order to evaluate the validity of the results.

Motivation

Over 11 billion tons of fossil fuels are consumed globally every year. The oil reserves are vanishing and the majority of it might be gone by 2052 [4]. This heavy decline in fossil fuel resources is an immense problem for our society, because until now these have been used as primary resource to generate electrical energy. At the same time, the world population is significantly increasing. Consequently, this leads to excessive energy consumption and an increase of emissions into the atmosphere. All in all, we are faced with the consequences of climate change. As a result, the main goal of the future will be on the one hand reducing the greenhouse related emissions, on the other hand changing the worldwide energy demand to maintain our standard of living and to assure quality of life for future generations. For this purpose, we have to find new ways to utilize available resources in a more efficient way. In other words, energy conversion should occur in an environmentally friendly and sustainable way.

In the last few years, research and development in sustainable energy technologies have been gaining importance. Especially energy conversion through electrochemical processes is going to play a key role in many different fields of technologies. In this respect, there is a strong need for materials which are very efficient for oxygen reduction reaction. In current situations though, the rate-limitation of the oxygen exchange kinetics by the surface exchange process represents a drawback for many technological applications. Consequently, recent efforts are motivated to improve the functionality of electrochemical systems.

Especially, mixed ionic and electronic conductors (MIECs) are gaining importance for energy conversion and storage, such as materials for solid oxide fuel and electrolyzer cells, ceramic membranes for selective oxygen separation, electrochemical high temperature oxygen sensors and heterogeneous catalysts. [3, 5]. Due to the fact that the electrochemically active site is part of the solid-gas interface, the reduction reaction is not limited to the length of triple phase boundaries. Therefore, MIEC-ceramics are stable at operating temperature with no or less polarization effects. For this purpose, K_2NiF_4 -type rare earth nickelates are among the most promising materials because of their favorable properties, such as high diffusivities, good electronic and significant ionic conductivities [3].

According to previous studies, $\text{Pr}_2\text{NiO}_{4+\delta}$ shows excellent performance for electrochemical applications but the oxygen exchange kinetics is limited by the surface exchange process [1, 6-9]. In the current work, Ni was partly substituted with cobalt with the intention to increase the surface exchange kinetics of oxygen.

This thesis focuses on the synthesis and characterization of the new Co-substituted praseodymium nickelate $\text{Pr}_2\text{Ni}_{0.9}\text{Co}_{0.1}\text{O}_{4+\delta}$. Chapter 1 will elucidate the primary motivation behind that work. In addition to that, it will give a theoretical background to all applied methods used for the characterization. Chapter 2 deals with main working steps, states experimental details and shows the experimental setup for all measurements. Chapter 3 will focus on the results and their interpretation. Finally, Chapter 4 gives the conclusions and an outlook.

1. Theory

To understand the basic concepts together with the motivation for perovskite related materials, it is necessary to discuss the structure and properties of nickelates and its related characterization techniques. Following chapter gives a theoretical background in more detail.

1.1. Rare Earth Nickelates

Rare earth nickelates based on oxides from the Ruddlesden-Popper series are promising materials for various applications. The most significant features of these nickelates are the fast oxygen diffusion and good catalytic properties (oxygen reduction reaction) due to their crystal structure and its related oxygen over-stoichiometry which is more closely examined below.

1.1.1. Crystal Structure

Generally, rare earth nickelate materials belong to the first member of the Ruddlesden-Popper series with the K_2NiF_4 structure, which adopt the general formulation [1, 3, 10]:



For the A-cation usually lanthanides or alkali, alkaline earth, or rare earth metals (La, Nd, Pr), and for the B-cation transition metals (Ni, Co, Fe) are used. According to equation 1, the crystal structure consists of two units: the perovskite and the rocksalt unit (Figure 1). Notation n is related to the number of octahedral (perovskite) layers between the AO layers.

The Goldschmidt factor (equation 2) defines the tolerance limit of cationic radii in the A and B sites.

$$t = \frac{(r_A + r_O)}{\sqrt{2}(r_B + r_O)} \quad (2)$$

r_A , r_B and r_O ... radii of the respective ions

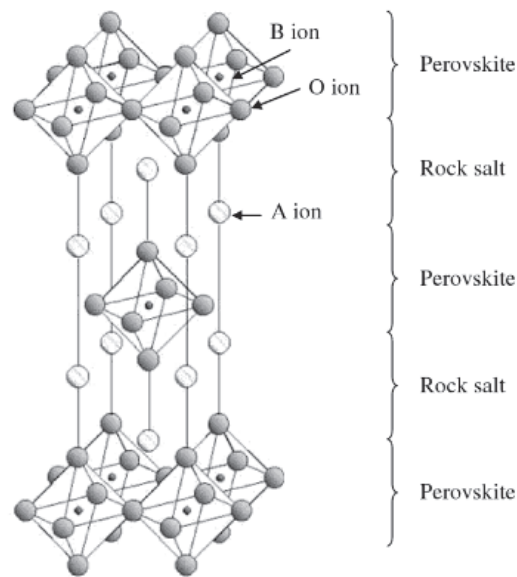


Figure 1: Schematic illustration of the crystal structure of K_2NiF_4 -type oxides [4]

Normally, the ionic radii of perovskite related structures are in relation $r_A \approx r_O > r_B$. In addition to that, the Goldschmidt factor, indicating the stability limit of the perovskite structure, should have a value between $0.75 \leq t \leq 1$. An ideal perovskite lattice (cubic unit cell) exists when $t = 1$ [11, 12]. Otherwise, a distortion of the lattice occurs, such as orthorhombic and rhombohedral distortion (Figure 2). These distortion or tilting effects on the BO_6 octahedra are caused by the fact that the A cation is larger in size than the B cation (placed in the interlayer octahedral interstices, $r_{ion,O^{2-}} = 140$ pm [13]).

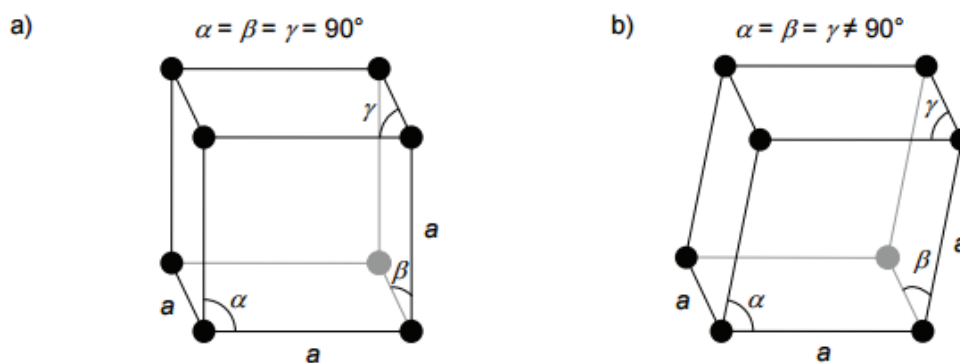


Figure 2: Principle of a cubic unit cell $t \approx 1$ (a), and a distorted elementary cell where $t \neq 1$ (b) [12]

The material presented in this thesis has praseodymium ($r_{ion,Pr^{3+}} = 113$ pm [13]) on position A, nickel ($r_{ion,Ni^{3+}} = 70$ pm [13]) and cobalt ($r_{ion,Co^{3+}} = 75$ pm [13]) on position B. The material crystallizes in an orthorhombic structure and the tolerance factor was calculated and lies

inside the stable range of $0,83 \leq t \leq 1$. The chemical formulation can be seen in following formula $\text{Pr}_2\text{Ni}_{0,9}\text{Co}_{0,1}\text{O}_{4+\delta}$. Here, δ gives information about the oxygen nonstoichiometry of the material. Non-stoichiometric materials have unbalanced quantities between reactants and products in the chemical reaction. As a result, they are usually good ionic conductors, whereas stoichiometric materials are often good isolators [3, 6].

Lanthanides like praseodymium are known for their existence in oxidation state +3 and +4. Due to that fact, electronic conductivity arises. Another consequence is the formation of oxygen vacancies/interstitials. Consequently, by increasing the number of oxygen vacancies or interstitials the ionic conductivity increases proportionally.

Nickel, a transition metal, is known for its good catalytic properties. It occurs in oxidation states +2 and +3 due to oxygen over-stoichiometry of the material. Oxygen excess and charge compensation occurs through oxidation of the B-site nickel cation. This property leads to a change or removal of the octahedral distortion by increasing the temperature or lowering the oxygen partial pressure (reduction of Ni^{3+} to Ni^{2+} - stabilization of the K_2NiF_4 structure). Consequently, electronic and ionic conductivity arises [6].

To increase the sintering activity as well as the oxygen exchange kinetics, the B-site position of the lattice was substituted with cobalt. A substitution was possible because the ionic radii of nickel and cobalt are very similar. Due to the flexibility of adopting different oxygen states (Co^{2+} , Co^{3+} or Co^{4+}), cobaltites are comparatively active to reduce oxygen. Especially Co^{3+} is well known for this special property. This flexibility leads to an oxygen nonstoichiometry, due to the possibility of intermediate valences in different crystal systems. Furthermore, cobalt enhances the electronic transport properties of oxide materials [2, 14]. Previous studies already showed that cobalt doped materials usually show an improvement in diffusion characteristics [15-18]. Kilner and Shaw [16] but also Munnings et al. [18] performed extensive studies to establish the surface exchange properties of materials based on $(\text{La})_2(\text{Co,Ni})\text{O}_{4+\delta}$. An increase in the Co concentration of $\text{La}_2\text{Ni}_{1-x}\text{Co}_x\text{O}_{4+\delta}$ (where $x \leq 0,5$) indicates an improvement of the surface exchange properties. The results show an enhancement of the surface exchange rate (Figure 3) but also a decrease in the activation enthalpy at low temperatures.

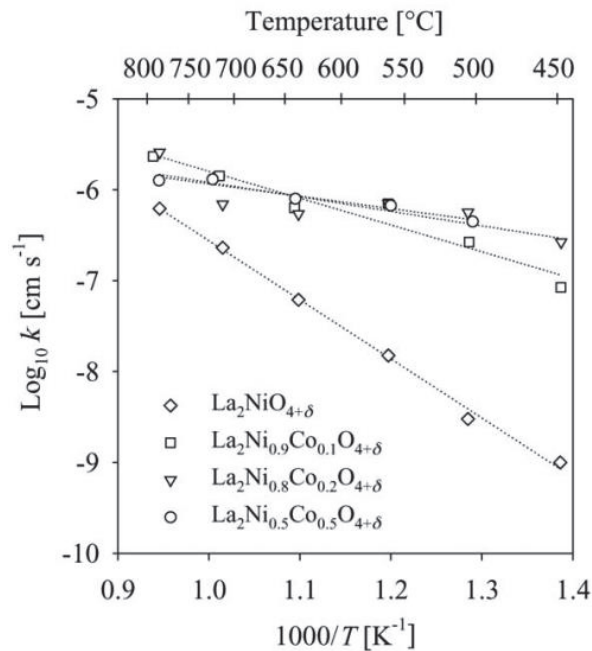


Figure 3: Surface exchange coefficients of $La_2Ni_{1-x}Co_xO_{4+\delta}$ at a nominal oxygen partial pressure of 200 mbar [16]

1.1.2. Diffusion Mechanism

The diffusion of oxygen is among the most important properties that characterize the quality of ceramic oxides. The principle task of future oxide materials is to process the chemical reduction reaction at low temperatures in an efficient way. For this purpose, it is necessary to have materials with high ionic and electronic conductivities and also favorable mechanical properties.

Oxygen diffusion usually occurs from a high to a low oxygen chemical potential. In case of the oxygen incorporation and transport through a bulk sample, the oxygen transfer occurs across the interface between the gas phase and the oxide [19]. In other words, oxygen is transported through the layer in the form of oxygen ions [11]. Equations 3 and 4 show the reduction reaction. The first part of the reaction represents the reduction of oxygen on the surface and the incorporation into the solid by consumption of a surface oxygen vacancy. The last part of

the reaction represents the transfer of oxygen through the material. In that case, the oxygen ion proceeds to diffuse [1, 3, 10].



In most solids diffusion takes place through atomic movements in the lattice by adding sufficient thermal energy. This leads to movements of atoms away from their equilibrium positions to a neighboring one. In oxide materials, oxygen diffusion usually occurs in three different ways: through interstitial, interstitialcy and vacancy hopping. Which mechanism takes place depends on the nature of the point defects in the crystal lattice. The interstitial mechanism is the diffusion of oxygen ions (solute atoms positioned at interstitial sites of the lattice) by moving from one interstitial site to a neighboring site (Figure 4, a). After completing a jump, all adjacent ions are not permanently displaced. Consequently, the interstitial atoms require less energy to migrate. They can move directly through the lattice, because they do not require the existence of defects in the lattice. The interstitialcy mechanism occurs, when the interstitial ion displaces another ion from its lattice position (displacement from its equilibrium state). The displaced ion has to move to a different interstitial site (Figure 4, b). The vacancy mechanism describes the migration of oxygen ions from their current position into neighboring vacancy sites (Figure 4, c). In this case, the presence of lattice vacancies (defects in the lattice) is an important precondition. By increasing the concentration of vacancies, the ionic conductivity increases proportionally as well. Precisely, it has a major impact on the kinetics of the material [20, 21].

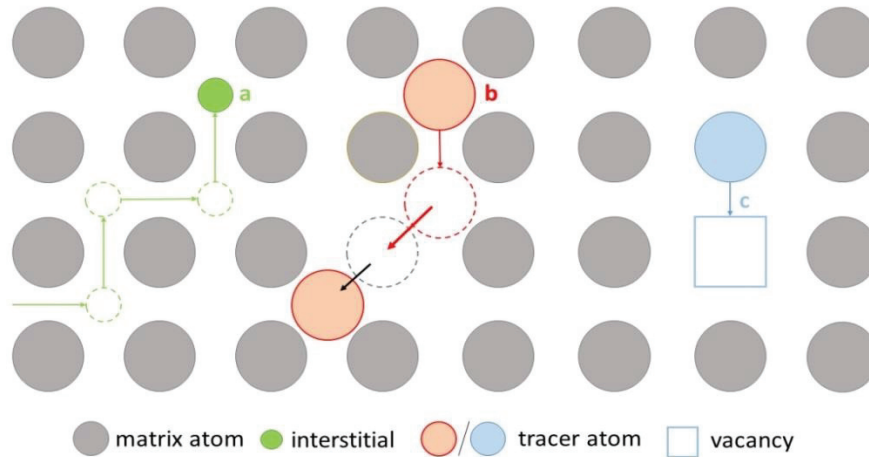


Figure 4: Oxygen diffusion in solids a) interstitial mechanism, b), interstitialcy mechanism, c) vacancy mechanism

The phenomenon of oxygen diffusion is described by the change in the Gibbs free energy (equation 5). The first part of equation Δh represents the energy E needed to form defects in the lattice. However, the last part Δs shows the increase in entropy due to the formation of defects. The value x symbolizes the mole fraction of defects [22].

$$\Delta g = \Delta h - T\Delta s = xE + RT(x \ln(x) + (1-x) \ln(1-x)) \quad (5)$$

According to Gellings [11] the oxygen diffusion requires the migration of atoms away from their equilibrium state. Consequently, Δg is limited to a minimum (equation 6 and 7).

$$\frac{\partial(\Delta g)}{\partial x} = 0 = E + R(\ln(x) - \ln(1-x)) \quad (6)$$

$$x = e^{\frac{-E}{RT}} \quad \text{if } x \ll 1 \quad (7)$$

How efficiently thermally activated oxygen ions can migrate through a lattice, depends on the height of the energy barrier (migration enthalpy). The Arrhenius equation (considering the Boltzmann relationship in equation 7) describes that oxygen ion exchange rate along the migration paths (equation 8-9) [11, 21, 22].

$$i = i_0 e^{\frac{-E_m}{k_B T}} \quad (8)$$

$$v = v_0 e^{\frac{-E_m}{k_B T}} \quad (9)$$

i...oxygen exchange rate of interstitials, *v*... oxygen exchange rate of vacancies, v_0/i_0 ...pre-exponential factor (constant), k_B ...Boltzmann's constant, E_m ...energy barrier along a migration path

Consequently, the oxygen diffusion coefficient D_O can be written as:

$$D_O = D_V * v + D_i * i = D_V [V_O^{\bullet\bullet}] + D_i [O_i^{\prime\prime}] \quad (10)$$

D_V ...vacancy diffusion coefficient, D_i ...interstitial diffusion coefficient, $V_O^{\bullet\bullet}$...concentration of oxygen vacancies, $O_i^{\prime\prime}$...concentration of interstitial oxygen

1.1.3. Diffusion in Oxygen-Deficient Materials

How efficiently oxygen vacancies or interstitials can be introduced into the nickelate compound depends on the chemical composition, the temperature and oxygen partial pressure, which leads to a nonstoichiometry of the material. The most significant factor is the A- and B-site doping. Depending on the doping-material, the nickelate can be either hypostoichiometric (oxygen deficient – existence of oxygen vacancies) or hyperstoichiometric (oxygen excess – existence of oxygen interstitials). Considering equation 9, the oxygen interstitial diffusivity D at a temperature T is:

$$D = D_i [O_i^{\prime\prime}] e^{\frac{-E_m}{k_B T}} \quad (11)$$

E_m ...energy barrier of migration, k_B ...Boltzmann's constant

For example, in perovskite ($ABO_{3-\delta}$) or fluorite ($AO_{2-\delta}$) structured materials oxygen diffusion occurs frequently through oxygen vacancy hopping as shown in Figure 5. The enhancement of the ionic conductivity can be obtained by increasing the defect charge carrier concentration. Thus, an increase in the formation of vacancies can be obtained by substituting the materials with an acceptor-dopant (A') or transition metal (B) due to their mixed valencies B^{3+} and B^{4+} .

In comparison, in materials with a potassium nickel fluorite structure (belonging to the Ruddlesden-Popper series of layered oxides), the diffusion of interstitial oxygen is predominant, through oxygen interstitials which are mobile in the AO layers [23].

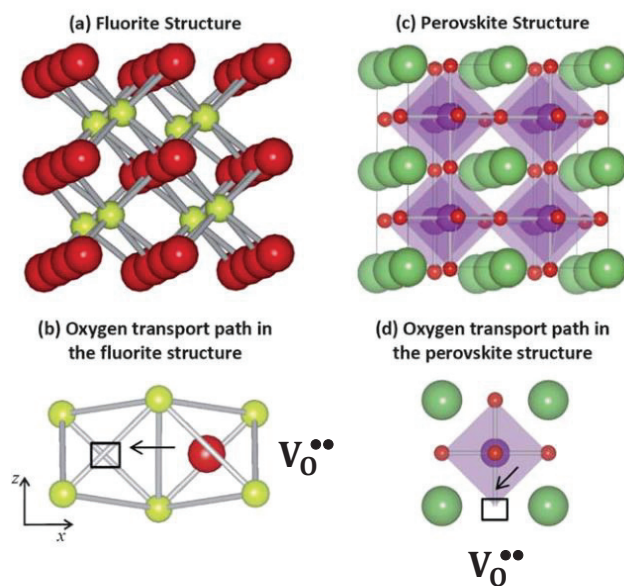


Figure 5: : Illustration of oxygen (red colored) diffusion by oxygen vacancy $V_O^{\bullet\bullet}$ hopping [20]:
 a) materials with fluorite structure
 b) materials with perovskite structure

This present work will concentrate on the first member of the Ruddlesden-Popper-series. Changes in stoichiometry and temperature have an impact on the polymorphs of the K_2NiF_4 structure.

1.2. Properties of Praseodymium Nickel Oxide

In contrast to the novel compound $\text{Pr}_2\text{Ni}_{0.9}\text{Co}_{0.1}\text{O}_{4+\delta}$ (PNCO), the properties of $\text{Pr}_2\text{NiO}_{4+\delta}$ (PNO) have been reported in several previous studies [1, 3, 24]. Due to the fact that the new material PNCO was substituted with only a small amount of cobalt, the assumption was made that the material properties would be relatively similar to $\text{Pr}_2\text{NiO}_{4+\delta}$. Figure 6 shows the phase diagram of PNO given by Sullivan, Buttrey [24]. It shows the stability fields for Pr-nickelates as a function of temperature and oxygen partial pressure. However, it needs to be mentioned that only the white points of the diagram shown in Figure 6 represent experimentally determined data. Consequently, the curve progression was linearly extrapolated. In air ($p_{\text{O}_2}=0.21$ atm), $\text{Pr}_2\text{NiO}_{4+\delta}$ is stable at temperatures below 780°C . For higher temperatures a transition to a higher Ruddlesden Popper phase and praseodymium oxide occurs ($\text{Pr}_4\text{Ni}_3\text{O}_{10}$ and PrO_x). The smaller the oxygen partial pressure p_{O_2} , the higher the probability of staying in the range of phase stability. However, at p_{O_2} lower than 10^{-7} bar the material reaches the Ni/NiO-reduction boundary. Below that threshold a reduction from $\text{Pr}_2\text{NiO}_{4+\delta}$ to metallic nickel and Pr_2O_3 occurs[1].

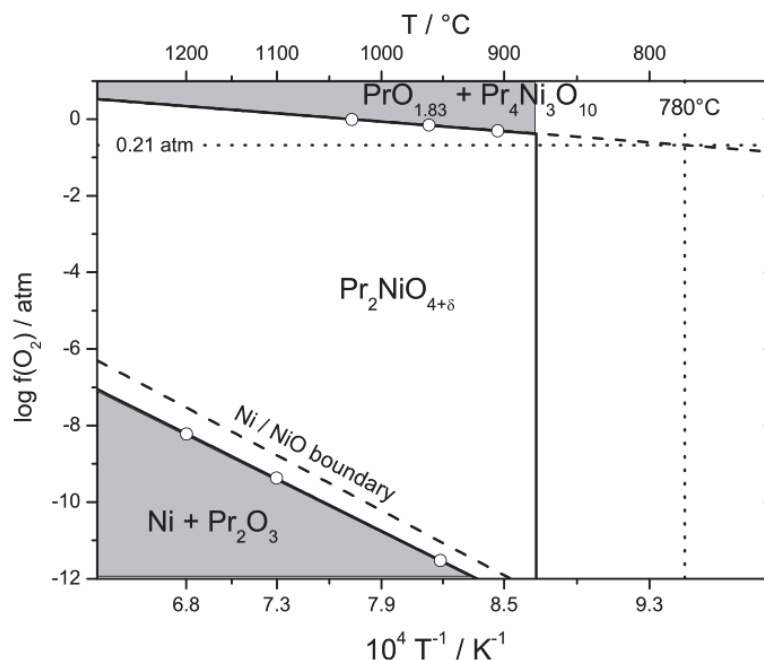


Figure 6: Phase diagram of $\text{Pr}_2\text{NiO}_{4+\delta}$ as a function of temperature and oxygen fugacity [1, 24].

Dotted lines visualize the decomposition temperature in air

1.3. Freeze Drying

Freeze drying is a process to remove ice or other frozen solvents from a material through sublimation. According to the phase diagram of water (see Figure 7), sublimation occurs when a solid (ice) changes directly to a vapor without first going through a liquid (water) phase. This phase change occurs by adding heat energy, a combination of the enthalpy of fusion and sublimation energy and reducing the pressure in the chamber [25, 26].

The main significant advantage over other synthesis methods is that during the freeze drying process the product temperature is kept low enough to avoid changes in the dried product appearance and characteristics. In addition to that, it is possible to obtain higher quantities of chemically homogenous, single phase powder in one batch.

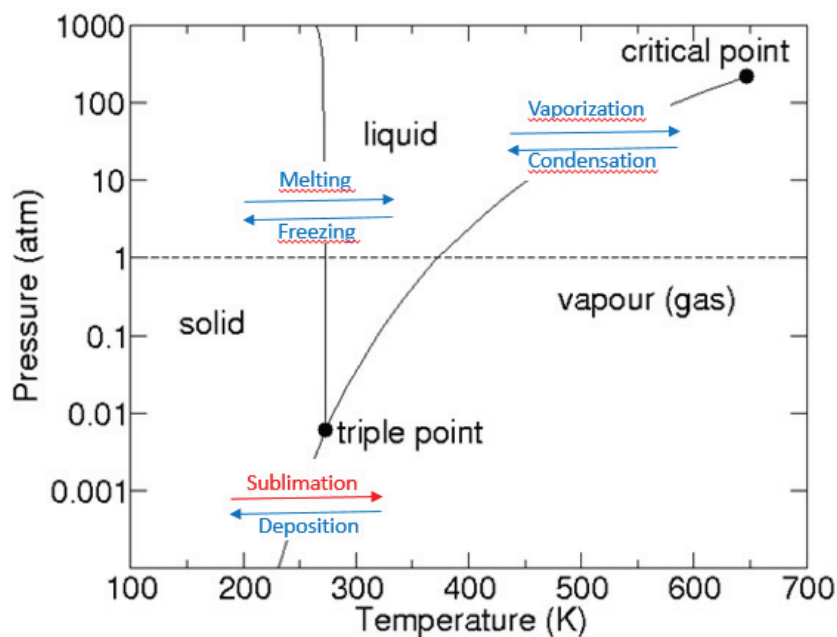


Figure 7: Phase diagram of water based on [27]

The freeze drying process consists of three main steps:

Pretreatment: Before starting the drying process, the aqueous acetate precursor solution has to be shock frozen. Unfrozen products expand when placed under a vacuum which should be avoided in the synthesis procedure.

Primary Drying: The product is placed under primary vacuum. Heat energy is added causing the ice to sublime. This has to be a very slow process. If too much heat is added, the structure of the material could be altered.

Secondary Drying: Although 95% of the ice will be disappeared at the end of the primary phase, the product is not sufficiently dry for long term storage. A small amount of frozen water remains. In the secondary phase, the temperature rises to break any physicochemical interactions between the water molecules and the frozen material.

For enabling the freeze drying process, the required heat supply can occur in two different ways: through a direct heat contact in the drying chamber or through radiation. Figure 8 shows a schematic representation of the sublimation process. Heat transfer occurs through contacting the vessel, filled with the previously shock frozen aqueous acetate precursor solution, with the heated shelves.

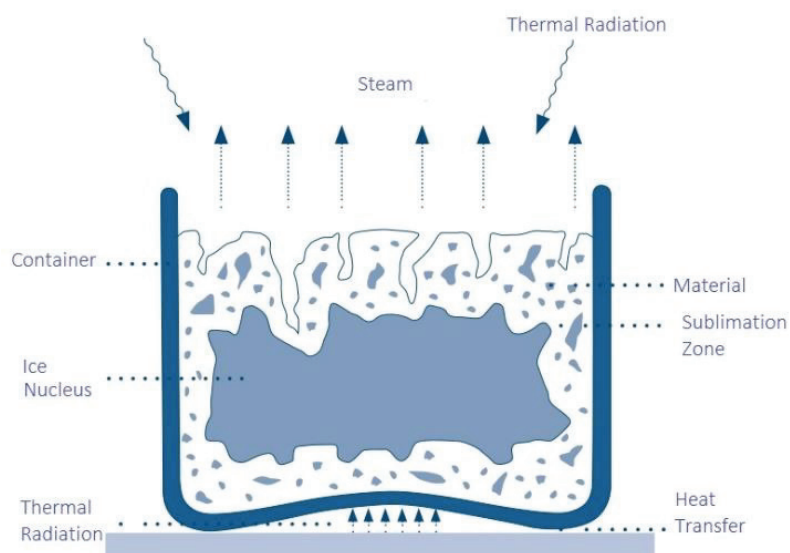


Figure 8: Illustration of freeze drying process [26]

Conversely, by using flasks for the freeze drying process outside the ice condenser chamber, heat transfer occurs through convection via the shelf and product. However, at the end of the primary drying nearly the whole material will be ice free, porous and dried. Due to the decrease in the heat conductivity of the already dried product, also the temperature of the ice core increases. The product now enters the desorption phase (secondary drying) to transfer the remaining evolved vapour to the condenser [25, 26].

1.4. Four Point dc-van der Pauw Technique

The van der Pauw method is a convenient technique used for resistivity measurements. By subjecting the sample to a fast pO_2 change and recording the corresponding change in the conductivity, the van der Pauw technique may also be applied to determine the oxygen exchange kinetics.

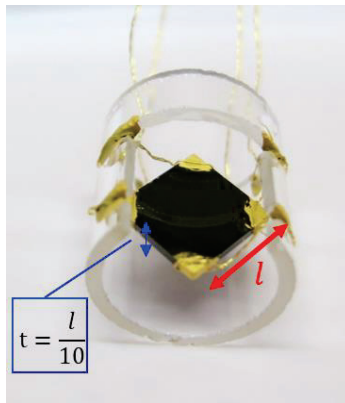


Figure 9: Sample assembled in specimen holder, t ...thickness, l ...edge length

In the van der Pauw measurement geometry an arbitrarily shaped (for example square) specimen is contacted on four points along the circumference (Figure 9). In contrast to linear four point dc-conductivity measurement setups, the exact positions of the four electronic contacts can be freely positioned on the circumference of the sample. More important is that the contacts are designed sufficiently small. Additionally, prerequisites for the investigated sample are plane parallel and highly polished surfaces and a constant thickness of the sample [1, 28].

If these criteria are fulfilled it may be assumed that oxygen diffusion only takes place vertical to the surface of the sample as shown in Figure 10. To avoid lateral diffusion, the thickness of the sample has to be one tenth of the edge length (reduction of the edge surface to avoid an oxygen exchange process) [1]. Oxygen diffusion takes place as follows: Oxygen molecules reach the reactive surface. The reduction reaction can occur by taking up two electrons to split

oxygen into oxygen ions O^{2-} . Finally, the oxide ions can diffuse through the dense electrode layer [2]. Thus, the chemical surface exchange coefficient (describing the kinetics of the exchange process on the surface of the sample), the chemical diffusion coefficient (describing the transport within the bulk), and the electrical conductivity can be defined. These three parameters govern the efficiency of the mass and charge transport kinetics of $Pr_2Ni_{0.9}Co_{0.1}O_{4+\delta}$.

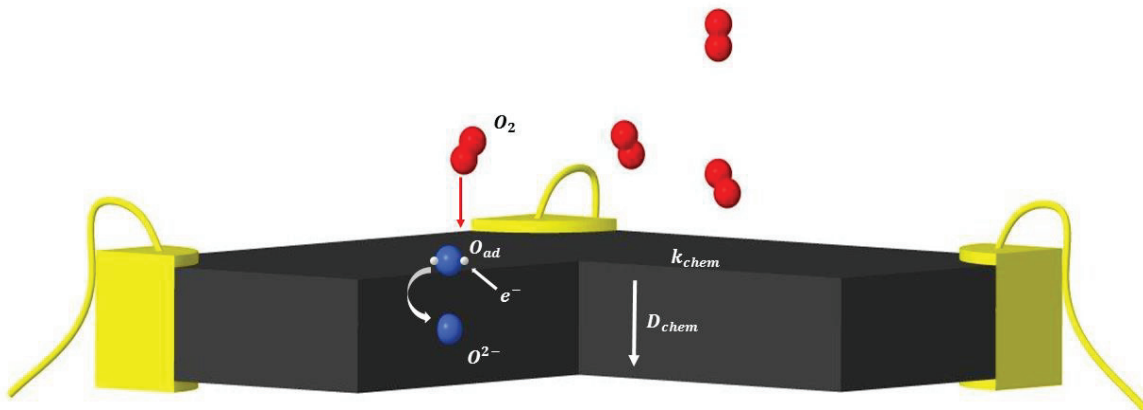


Figure 10 : Oxygen reduction process on the surface of the bulk sample, characterized by k_{chem} ...chemical surface exchange coefficient, and oxygen diffusion in the bulk, characterized by D_{chem} ...chemical diffusion coefficient

1.4.1. Electrical Conductivity Measurement

Two measurements are performed (see Figure 11): Current (100-500 mA, depending on the sample resistance) is applied to two adjacent sides of the sample and the voltage is measured at the opposite sides of the current contacts. In the second measurement the connections are reversed to eliminate thermal offsets. In this way, it is possible to determine the conductivity by combining the two resistance measurements and the thickness of the sample (equation 12-14) [28].

According to van der Pauw theory, the correlation between the respective resistances can be written as [1, 28]:

$$e^{-\pi t \sigma \frac{V_{43}}{I_{12}}} + e^{-\pi t \sigma \frac{V_{23}}{I_{14}}} = 1 \quad (12)$$

$$e^{-\pi t \sigma R_A} + e^{-\pi t \sigma R_B} = 1 \quad (13)$$

$$\frac{1}{\sigma} = \frac{\pi t}{\ln(2)} \frac{R_A + R_B}{2} f(r) \quad (14)$$

*t...*thickness of the sample, *σ...* electrical conductivity, function *f(r)* depends on the ratio of R_A and R_B , for V_{xx}/R_A and I_{xx}/R_B see Figure 11

Generally, the van der Pauw equation can only be analytically solved if $R_A = R_B = R$. In the case that R_A and R_B are equal (switching the contacts in full circle, more precisely after a 180° rotation of the contacts), $f(r)$ in equation 14 can be neglected (attains a value of 1) [1, 28]. Finally, the electrical conductivity can be calculated as

$$\sigma = \frac{\ln(2)}{\pi t R} \quad (16)$$

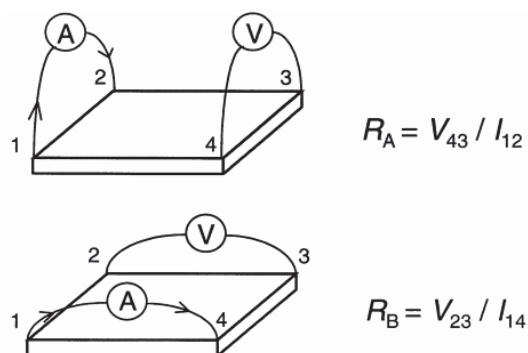


Figure 11: Van der Pauw geometry, $R...$ Resistance, $V...$ measured voltage, $I...$ applied current [28]

1.4.2. Conductivity Relaxation Measurement

During the conductivity relaxation measurement a current (100-500 mA, depending on the sample resistance) is applied and the voltage is measured. In order to determine the kinetic parameters for oxygen exchange, experiments are performed in a controlled atmosphere (for example using two defined gas mixture of O₂ and Ar) as a function of temperature. First, the sample is equilibrated in the surrounding atmosphere (balance between oxygen supply and consumption). Due to a step-wise variation of the oxygen partial pressure the electrical conductivity of the sample changes and relaxes to a new equilibrium state, Figure 12. According to Egger [4], the pO₂-steps should be as small as possible to ensure the significance of the characteristic values. This relaxation effect is based on an oxygen incorporation or release of the oxide material depending on the direction of the pO₂ change in the gas phase.

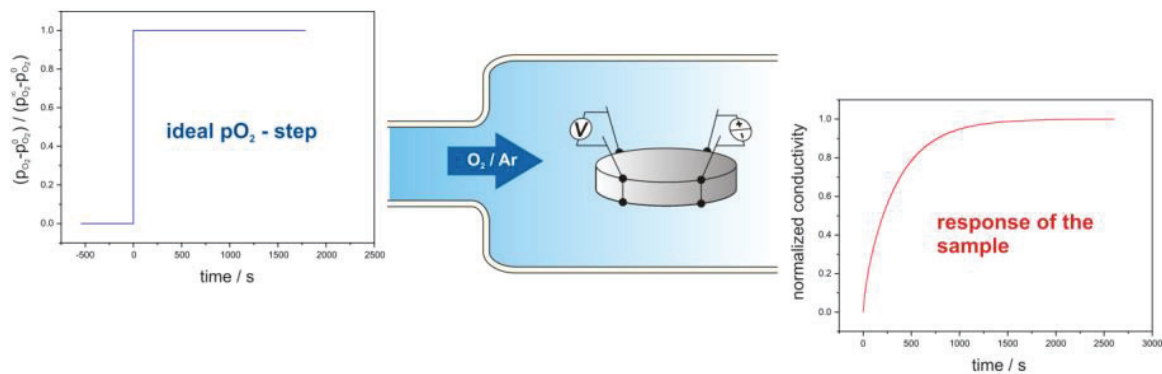


Figure 12: Illustration of the conductivity relaxation measurement process. At the beginning of the measurement the sample is in an equilibrium state. Changing the oxygen partial pressure (blue chart) causes a change in electrical conductivity (response of the sample, red chart) [1]

The diffusion mechanism is described by combining Fick's first law and the continuity equation (equation 16). The continuity equation describes the mass flux \vec{J}_O of oxygen through the sample (link between changes in the charge density c_O and the electrical current).

$$\frac{\partial c_O}{\partial t} = -\nabla \vec{J}_O \quad (16)$$

This relaxation process can be modeled by the following two equations (17-18).

$$\frac{\partial c}{\partial t} = D_{chem} \nabla^2 c \quad (17)$$

$$J = k_{chem} (c_s(t) - c_\infty) \quad (18)$$

J ...flux through the layer, $c_s(t)$...time dependent surface concentration of oxygen, c_{oo} ... equilibrium oxygen concentration after the relaxation process

For both equations the assumption was made that the diffusion coefficient and the surface exchange coefficient remain constant during the relaxation process.

Furthermore, the tracer surface exchange coefficient k^* (describes particle interaction on the surface) and the chemical surface exchange coefficient k_{chem} are related by a correlation factor γ shown in equation 20. This factor describes the deviation of the diffusing oxygen ions from its random walk. An analogous relation applies to the chemical diffusion coefficient D_{chem} [2].

$$k_{chem} = \gamma k^* \quad (19)$$

$$D_{chem} = \gamma D^* \quad (20)$$

According to Granger, Parvulescu [2], the critical length of the sample is defined as follows

$$L_c = \frac{D_{chem}}{k_{chem}} \quad (21)$$

D_{chem} ...chemical diffusion coefficient, k_{chem} ...chemical surface exchange coefficient, L_c ...critical length

This parameter, in relation to the thickness L of the sample, indicates the different control regimes, which can be classified in surface controlled, diffusion controlled and mixed controlled (Figure 13) [1].

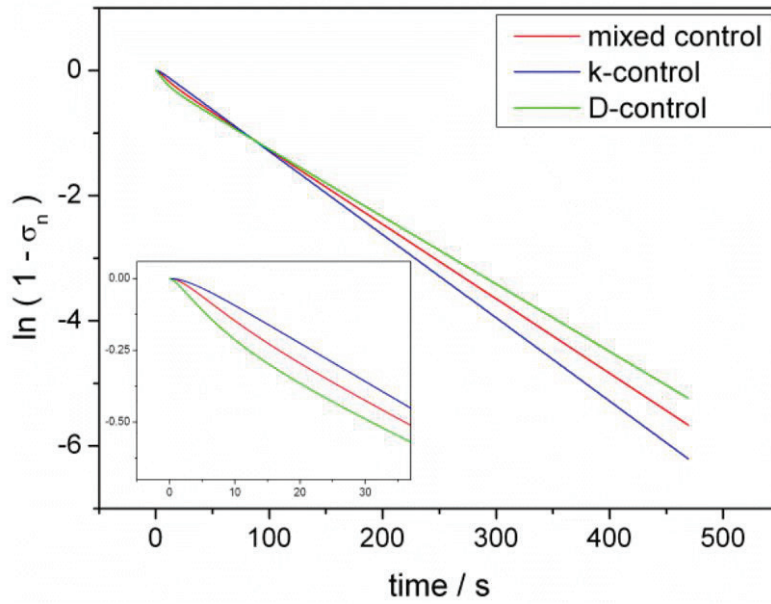


Figure 13: Conductivity transients of relaxation measurements (one-dimensional oxygen exchange and semi logarithmic axis). Illustration of the different relaxation process regimes (red: mixed controlled, blue: k-controlled and green: D-controlled) [1]

Due to the fact that $\text{Pr}_2\text{Ni}_{0.9}\text{Co}_{0.1}\text{O}_{4+\delta}$ shows a k-controlled behavior (linear curve progression of the semi-logarithmic representation of the conductivity relaxation transients shown in Figure 13), the following section only provides detailed information of the derivation of the surface exchange coefficient k_{chem} .

As mentioned in equation 18, the surface exchange process is usually assumed to follow a linear rate law and describes the relation between oxygen flux J_O and the deviation of the oxygen concentration from the equilibrium value c_∞ (equation 22).

By using equation 18 and integrating over the total samples Volume V (obtaining mass flux of oxygen) it is possible to determine the surface exchange coefficient and equation 18 simplifies to

$$\iiint_V \frac{\partial c}{\partial t} dV = - \oint_A \vec{j} \cdot d\vec{A} \quad (22)$$

$$\frac{dc}{dt} V = -k(c(t) - c_\infty)A \quad (23)$$

A...total sample surface

If equation 23 is solved with the initial condition ($c(0) = c_0$) the average concentration of oxygen \bar{c} inside the sample at time t can be written as

$$\bar{c}(t) = \frac{c(t) - c_0}{c_\infty - c_0} = 1 - e^{-k \frac{A}{V} t} \quad (24)$$

The van der Pauw geometry only allows oxygen diffusion normal to the samples' surface planes. Thus, interstitial oxygen flows through the two opposite plane parallel surfaces (see Figure 10). Finally, the above-mentioned equation yields

$$\bar{c}(t) = 1 - e^{-k \frac{2}{L} t} \quad (25)$$

This equation applies only when the oxygen exchange process is solely described by equation 18. In other words, diffusion is assumed to be infinitely fast (k -controlled behavior, $D_{chem} \rightarrow \infty$). Finally, the conductivity relaxation transient can be written as

$$\sigma_n = 1 - e^{-\frac{2}{L} k_{chem} t} \quad (26)$$

By executing a nonlinear regression, using equation 26 of the conductivity relaxation transient, the surface exchange coefficient k_{chem} can be obtained (fitting parameter).

1.5. X-Ray Diffraction

X-ray diffraction is frequently applied for investigating crystal structures. The scales of these structures are similar to the wavelength of X-ray radiation. Therefore, diffraction can be observed under certain circumstances. For constructive interference the angle of the incident beam has to be equal to the angle of the diffracted beam (the net plane's normal vector is parallel to the scattering vector) as shown in Figure 14 and Figure 15, and Bragg's law (equation 27) has to be fulfilled. It gives the relation of the lattice constant, the X-ray's wavelength and the angle of the diffracted beam for constructive interference. By measuring this angle at a certain wavelength the lattice constant can be calculated [29, 30].

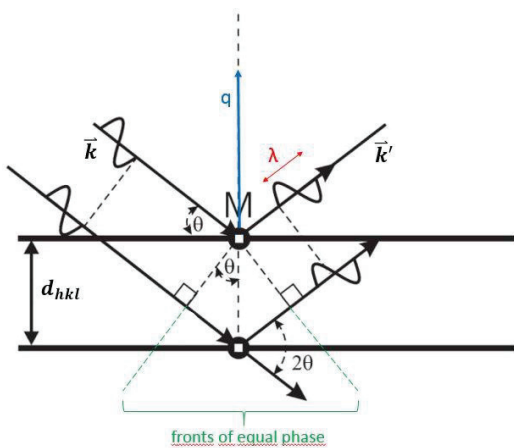


Figure 14: X-ray diffraction: k ...incident beam; k' ...diffracted beam; q ...scattering vector; θ ...diffraction angle; d_{hkl} ...lattice constant of hkl -plane [31]

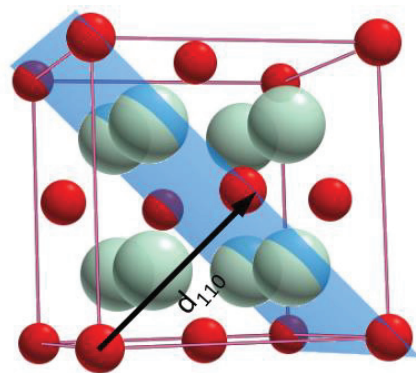


Figure 15: d_{hkl} ... lattice constant of hkl -plane- geometric function of size and shape of a unit cell [30]

$$n \lambda = 2 d_{hkl} \sin(\theta) \quad (27)$$

d_{hkl} ... lattice constant of hkl -plane; λ ... X-ray wavelength; θ ... diffraction angle

By measuring the intensity of the diffracted beam (investigating all crystal's net planes) as a function of its angle, properties of an unknown material can be found ($\theta/2\theta$ measurement). The results can be compared to reference values for gaining information about the molecular components and structure [29, 30].

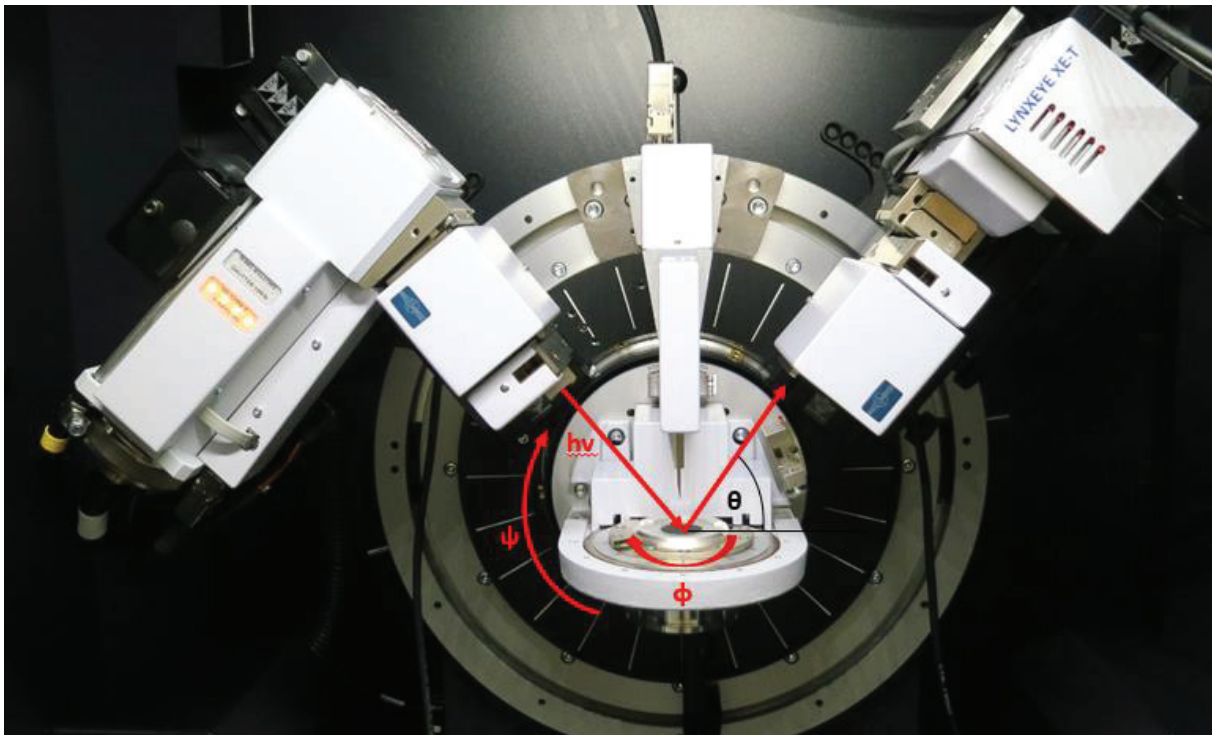


Figure 16: Bruker 8D Advanced: θ ... adjustable angle fulfilling Bragg's Law, Φ ... adjustable rotation angle (sample holder), Ψ ...adjustable tilting angle (sample holder), h ...Planck constant, v ... frequency of the photons absorbed or emitted

The crystallites of a material might have a preferred direction. Therefore, the measured diffracted intensity varies when keeping the 2θ angle constant and altering the Ψ (tilting the sample, see Figure 16) or the Φ (rotating the sample) angle. A scan over the whole range of such an angle in order to find the highest intensity is called "rocking curve".

A pole figure is recorded when altering the Φ ($0^\circ - 360^\circ$) and Ψ ($0^\circ - 90^\circ$) angle at a fixed $\theta/2\theta$ angle. The θ angle has to be set to a certain value which fulfills Bragg's law for a specific net plane. Peaks of intensity in the pole figure are recorded when the net plane's normal vector is parallel to the scattering vector [29]. The law of Beer-Lambert (equation 28) is used to calculate intensities:

$$I = I_0 \cdot e^{-\mu t} \quad (28)$$

I ...resulting intensity, I_0 ...initial intensity, μ ...absorbance of the material,
 t ...thickness of the absorbing material

1.6. Thermal Analysis

Table 1 contains frequently applied measurement methods to investigate the thermal stability of nickelates or any other materials of interest. Following section will give a brief introduction to the theoretical background of each characterization technique.

Table 1: List of different measurement methods to characterize thermal properties

Method	Acronym	Measured property	Object of investigation	Instrument
Dilatometry	DIL	Length change	thermal expansion	Netzsch DIL 402 PC
Thermogravimetric Analysis	TG	mass change	decomposition reactions solid/gas reactions	Thermobalance Setaram TAG 16
Differential Scanning Calorimetry	DSC	heat flow	heat of transition, change in specific heat	Netzsch DSC 404 PC

1.6.1. Dilatometry Analysis (Thermal Expansion Coefficient)

Thermal expansion is based on the physical principle that solid materials expand upon heating due to the increase in the specific volume of crystals. Depending on the type of material and the temperature program, different substances expand to a different extent. The coefficient of thermal expansion α is a common material key figure that indicates the extent to which a material expands upon heating. It defines the fractional length increase per unit rise in temperature shown in equations 29-31 [32].

$$\frac{l-l_0}{l_0} = \alpha (T - T_0) \quad (29)$$

$$\frac{\Delta l}{l_0} = \alpha \Delta T \quad (30)$$

$$\alpha = \frac{1}{l_0} \frac{\Delta l}{\Delta T} \quad (31)$$

l...actual length of the sample, *l*₀...original length (t=0), *T*...actual temperature, *T*₀...original temperature (t=0)

Dilatometric analyses (DIL) are widely used to obtain α (Figure 17). With this technique the material (compacted powder or sintered sample) is heated up, causing a volume (length) change (shrinking in case of a sintering process observed on a compacted powder sample, expansion in case of a sintered sample). A sensor (push rod) perceives resulting deformations by measuring the change of the sample length [33].

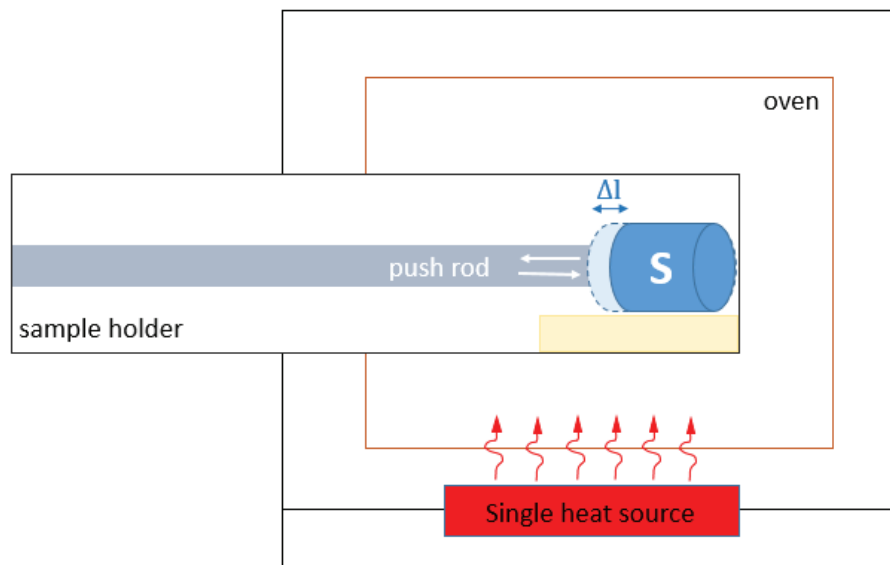


Figure 17: Schematic representation of functionality of a dilatometer, based on [33]

Generally, the thermal expansion coefficient α is a very important parameter to verify the compatibility between oxide ceramics to other materials. In fuel cell stacks, for instance, the electrical connection between the electrochemical cells is provided via interconnects. In terms of chemical stability and mechanical compliance the expansion properties have to be compatible with other materials. Another example would be the matching of thermal expansion coefficients between electrode materials and electrolytes to avoid delamination effects [3, 10].

1.6.2. Thermogravimetric Analysis

Thermogravimetric analysis (TG) is a very effective method to obtain the physical and chemical properties of a material as a function of temperature, time and atmosphere. Primarily, this technique can characterize materials' phase composition and predict their thermal stability.

During the measurement the sample temperature is varied according to a controlled temperature program. The program can be either isothermal ($T(t) = \text{const.}$) or nonisothermal. Usually, the heating rate is kept constant (see equation 32) by changing the temperature linearly with time during the nonisothermal program [34, 35].

$$\beta = \frac{dT}{dt} = \text{const} \quad (32)$$

Non-stoichiometric materials with a K_2NiF_4 structure ($A_2BO_{4+\delta}$, $A=(La,Pr,Sr,Ca,Ba)$, $B=(Co,Fe)$, $\delta=f(x,T, pO_2)$) have unbalanced quantities between reactants and products in the chemical reaction. Due to the fact that oxygen ceramics take up or release oxygen at high temperatures it can be concluded that the nonstoichiometry is directly related to the mass change of the material (equations 33-35 [36]).



$$\Delta\delta = \delta_0 - \delta_\infty = \frac{n_O}{n_{A_2BO_4}} = \frac{\Delta m \times M_{A_2BO_4}}{m \times M_O} \quad (35)$$

Phase transformations which are coupled to a mass change (for example transitions from the K_2NiF_4 structure to higher Ruddlesden-Popper phases) can be determined by measuring the weight increase or decrease upon heating and cooling of the material. In addition, the measurements can be performed in controlled gas atmospheres (static or dynamic), for instance oxidizing conditions (reactive gas for instance 20% oxygen, rest argon) or inert conditions (argon or helium) [34]. The process of the TG-experiment is illustrated in Figure 18.

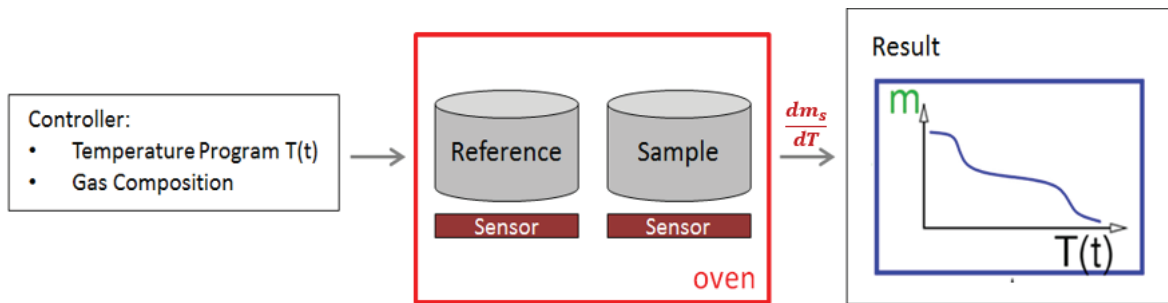


Figure 18: Process TG experiment, measurement of the mass change by varying the temperature

Figure 19 shows the difference in results of several TG experiments given by Egger [1]. The curve progression is directly related to the stability of the compounds. The reversible shape of the curve ($\text{La}_2\text{NiO}_{4+\delta}$ and $\text{Nd}_2\text{NiO}_{4+\delta}$) indicates chemical stability (state of equilibrium; oxygen loss upon heating, oxygen uptake upon cooling). Conversely, the irreversible mass curve is an indication of phase instability ($\text{Pr}_2\text{NiO}_{4+\delta}$). The latter usually occurs due to the irreversible incorporation of oxygen in the course of the phase decomposition of the K_2NiF_4 type compound into a higher Ruddlesden Popper phase). In pure argon (curve not shown) no mass increase is visible. This is expected because there is no oxygen available in the surrounding atmosphere. Consequently, no oxygen is absorbed by the material.

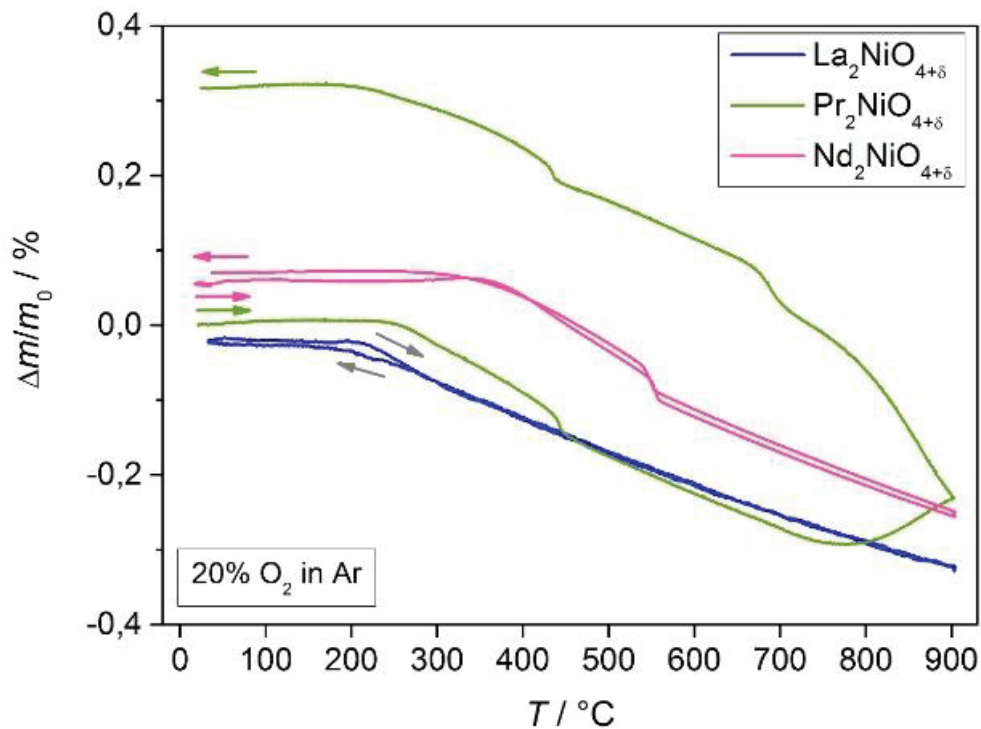


Figure 19: TG curves of different rare earth nickelates [1]

1.6.3. Differential Scanning Calorimetry

The main objective of differential scanning calorimetry (DSC) is the measurement of heat effects. The principle of the method is the comparison of an investigated material and a reference upon heating (Figure 20) [37]. During the experiment the furnace is heated (linearly in time) and heat H flows through the sample and reference (equation 36). The differential temperature signal ΔT is recorded (heat flux versus temperature or time).

$$\Delta \frac{\partial H}{\partial t} = \left(\frac{\partial H}{\partial t} \right)_{\text{sample}} - \left(\frac{\partial H}{\partial t} \right)_{\text{reference}} \quad (36)$$

In the case of thermal effects occurring in the sample, the reference heats faster or slower than the sample. Thus, when the sample undergoes a physical or phase transformation, more or less heat will be needed to flow through the sample than through reference. The deviation of the heat flow of the sample and reference can be either exothermic or endothermic. During endothermic processes (for instance release of oxygen from K_2NiF_4 -type oxides) heat is absorbed. As a result, the heat flow through the sample is higher than that through the reference, therefore $\Delta \frac{\partial H}{\partial t}$ is positive. Hence, the exothermic process $\Delta \frac{\partial H}{\partial t}$ is negative (absorption of oxygen) [37].

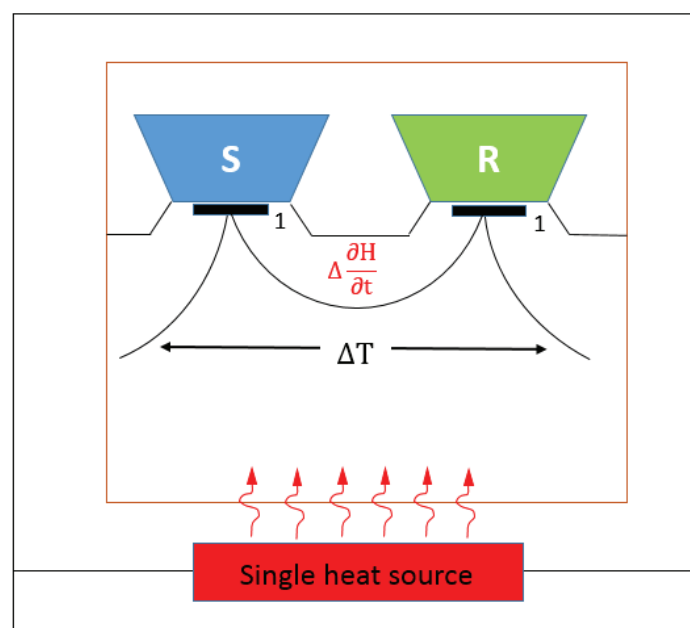


Figure 20: Illustration of the DSC measurement procedure, based on [37]

S...sample, R...reference, 1...differential thermocouples, ΔT ...differential temperature signal

2. Synthesis and Preparation of a Dense PNCO Sample

The following flow charts shows the main working steps from the very beginning of the experimental procedure (synthesis, sample preparation, contacting, ...) to the characterization of PNCO through appropriate measurements. The following chapter will focus on the detailed description of the workflow.

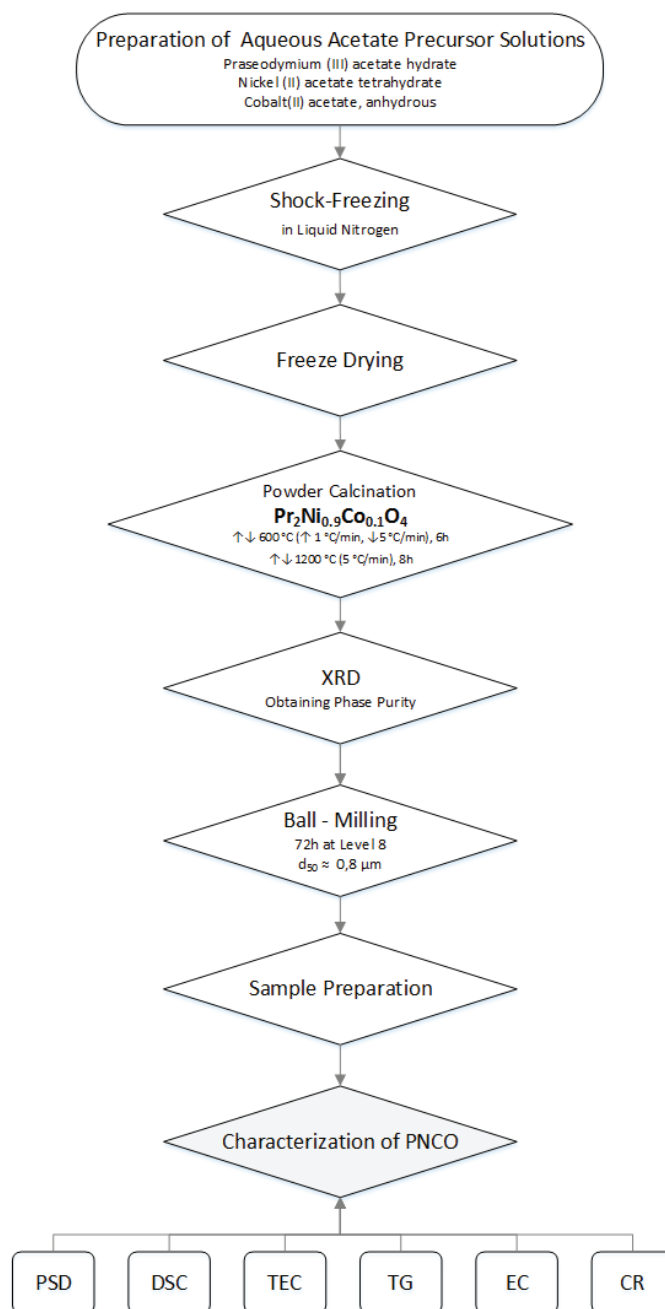


Figure 21: Synthesis and characterization of $Pr_2Ni_{0.9}Co_{0.1}O_{4+\delta}$ – Overview

2.1. Material Synthesis

Homogeneous single-phase PNCO powder was synthesized via freeze drying. All of the freeze drying process' steps are bundled together in one diagram (Figure 22) described in more detail below.

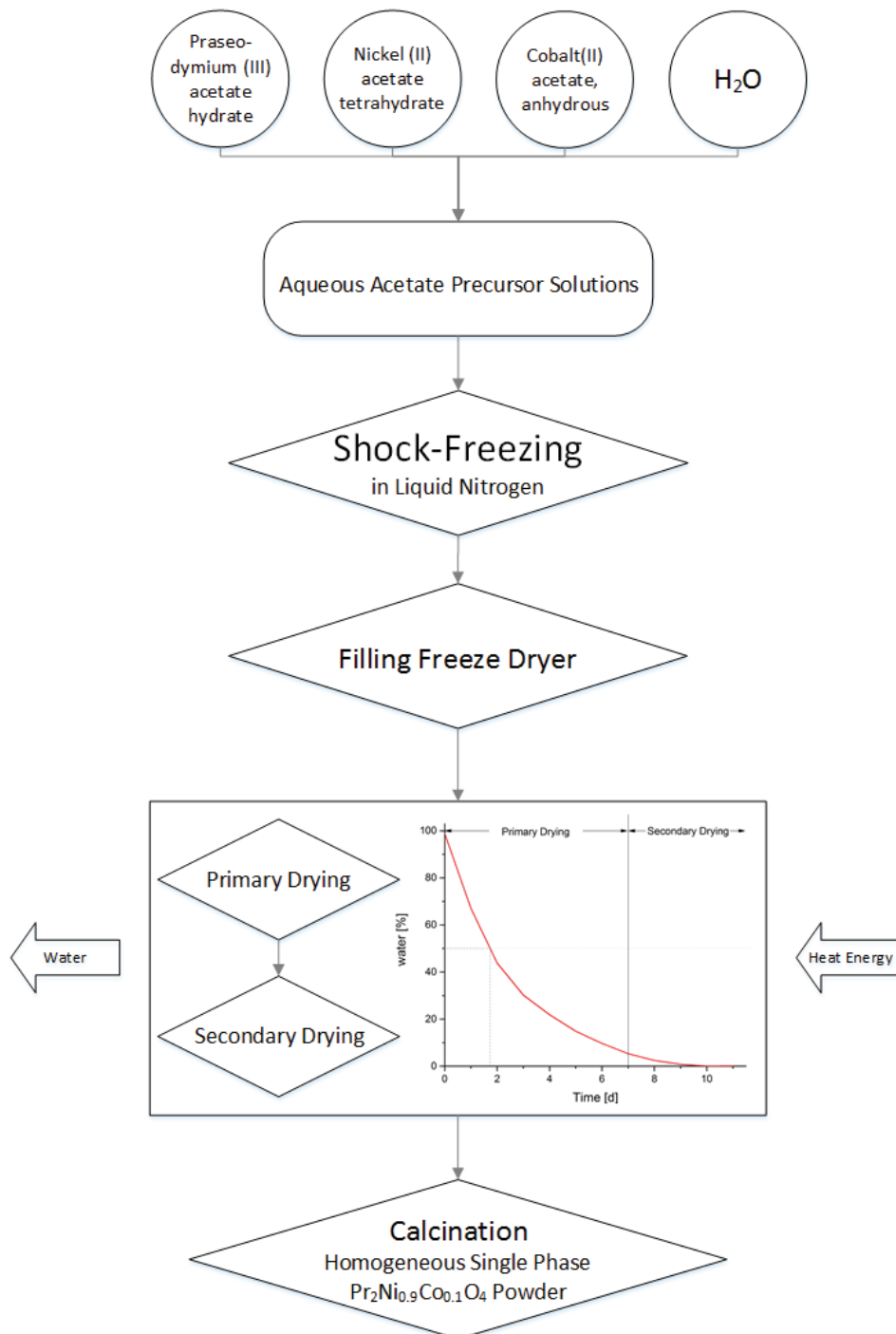


Figure 22: Overview Synthesis Process

Before starting the process the aqueous metal acetate solutions had to be mixed in a correct ratio in order to obtain the K_2NiF_4 -type oxide. The composition can be seen in Table 2.

Table 2: Composition of aqueous metal acetate solution

c... concentration, x_i ... mole fraction, t ... titer, V ... volume, n ...amount of substance

Acetate	x_i [mol%]	c $\left[\frac{\text{mol}}{\text{l}}\right]$	t	V [ml]	n [mol]
Pr	2.0	0.3	0.88302	700.00	0.185434
Ni	0.9	0.5	1.01120	165.04	0.083445
Co	0.1	0.2	0.91195	50.83	0.009272

As mentioned in Chapter 1.3, the solution has to be shock-frozen before starting the drying process to avoid any product's losses or a contamination of the freeze dryer (model ALPHA 1-2 LD plus). Figure 23 shows the experimental setup for the shock freezing. A rotary vane pump continually pumped the solution through a thin needle onto the surface of the liquid nitrogen. As long as the beam was injected under pressure, the solution froze to a fine granulate immediately. To achieve this, the needle had to be placed close to the nitrogen's surface and the beam was injected into the opposite direction of the nitrogen's rotation (evoked by an agitator to avoid an agglutination of the granulate).



Figure 23: Freeze drying setup – shock-freezing in liquid nitrogen

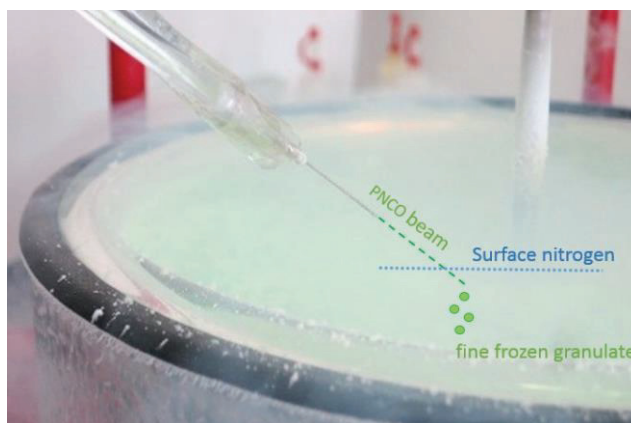


Figure 24: Freeze drying process

Immediately after the shock freezing process the frozen material was placed into a fridge to allow the evaporation of residual nitrogen. The following procedure steps were performed very quickly to avoid the thawing of the product. Even the smallest amount of unfrozen water molecules can have a significant impact on the phase composition of the material. By increasing the amount of unfrozen material fractions, the phase purity decreases. Consequently, all used equipment, for instance beakers, round bottom flasks, a funnel, spoons, etc., were cooled previously.

Then, the freeze dryer was filled (see Figure 25) and the primary drying was started. Figure 25-27 shows the difference between the appearance of the precursor solution at the beginning of the primary drying period (7 days) and the end of the secondary drying period (3 days). There was a significant reduction in the volume. This is attributable to the previously described sublimation process during the freeze drying process. In the end, all the ice was removed.



Figure 25: Fully laden ALPHA 1-2 LD plus freeze dryer



Figure 26: Beginning of the primary drying

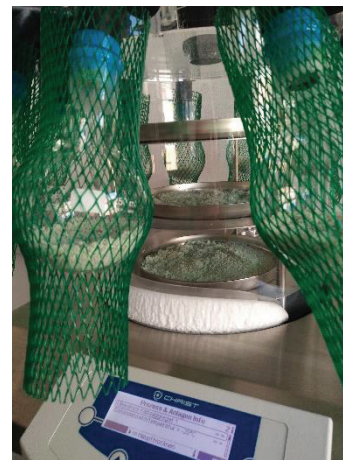


Figure 27: End of secondary drying

For subsequent processing, the freeze-dried acetate powder was calcined. During the calcination step, the acetates decomposed into the binary oxides. Then the solid-state reaction takes place between the constituents resulting in the desired phase and the complex K_2NiF_4 oxide was formed. Therefore, it was necessary that the calcination was performed at the right temperature to obtain the best electrical and mechanical properties and to avoid any phase decomposition. In table 3 the calcination program is listed.

Table 3 : Calcination program

T...temperature, Ramp... heating up and cooling down rate, Hold...holding upper temperature limit

#	T [°C]	Ramp	Hold
1	600	\uparrow 1°C / min \downarrow 5°C / min	6 Hours
2	1200	$\uparrow\downarrow$ 5°C / min	8 Hours

2.2. Milling Process

A small particle size is necessary to ensure a high relative density of the PNCO pellet. Consequently, the powder has to be ball milled. Ball milling is an efficient way to crush wet or dry powders into finer particle sizes (Figure 28). As milling media ZrO_2 balls ($d=3$ mm) were used. The ideal ratio (equation 37) between the milling components is:

$$1\text{g powder} : 7,7\text{g } ZrO_2 \text{ – balls} : 6\text{g EtOH} \quad (37)$$

The milling process was executed for 72 hours. Subsequently, the particle size was determined by a Particle Analyzer based on laser-diffractometry (Cilas 1064). The result illustrated in Figure 29 shows a monomodal distribution and average particle size of $\sim 0,65 \mu\text{m}$.

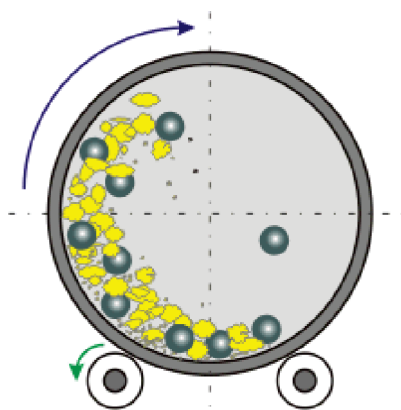


Figure 28: Schematic process of ball milling, grey... ZrO_2 -balls,... yellow... powder [38]

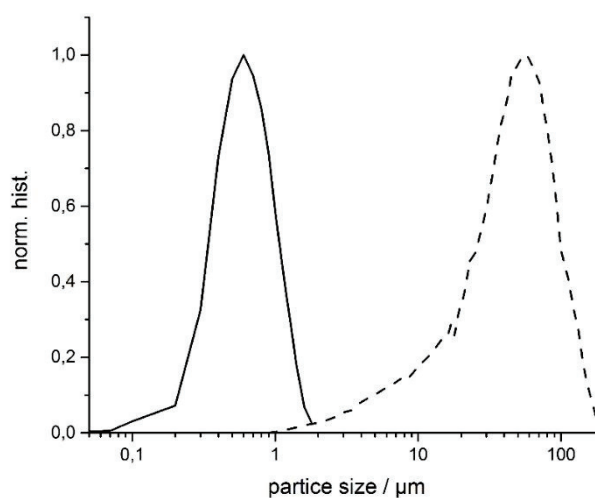


Figure 29: Particle size of the powder after 75h milling, dashed line... particle size before the milling process

2.3. Sample Preparation According to van der Pauw

For dc-conductivity and conductivity relaxation measurements a high relative density (ratio of the actual density and theoretical one) is required. The relative density is a measure for the porosity in a sintered body, which in turn has a significant effect on the properties of ceramic composites and can lead to errors in the measured material properties. For instance: an increase in porosity (non-conducting) leads to an apparent decrease in electrical conductivity. However, the oxygen diffusion coefficient apparently increases due to the fact that gas phase diffusion takes place faster than the solid state one [10].

To produce a dense pellet the powder was isostatically pressed (P/O Weber 30 S - manuell) in a cylindrical rubber mold to obtain a regularly shaped form ($F = 250$ MPa, 25 min). Subsequently, the pellet was sintered. Sintering is a process of densification by solid state diffusion at high temperatures. The PNCO powder got compacted and densified.

The geometric density was calculated by using the mass and dimensions of the sintered sample. By using the theoretical density, investigated through the crystal structure (XRD), the relative density was determined. For comparison, another pellet was produced consisting of Co-free PNO. The pellet was produced, sintered and processed under same conditions as PNCO. In Table 4 the different sintering programs, calculated and measured densities and the dimensions of the sintered bulk sample (Figure 30 a) are listed.

Table 4: List of sintering program, pellet's dimensions and densities

T_s ... sintering temperature, δ_{theor} ... theoretical density from XRD, δ_{bulk} bulk density,

δ_{rel} ... relative density, sintering shrinkage... comparing the dimensions of the sample before and after the sintering process

	PNCO291_01 (decomposed)	PNCO291_02	PNO
T_s [°C]	1120	1200	1300
ramp	↑↓ 2°C/min, 10h	↑↓ 5°C/min, 2h	↑↓ 2°C/min, 2h
ρ_{theor} $\left[\frac{\text{g}}{\text{cm}^3}\right]$	7.34	7.34	7.34
h [mm]	5.41	1.69	6.03
d [mm]	4.35	10.27	12.27
m [g]	0.58	0.99	4.97
ρ_{bulk} $\left[\frac{\text{g}}{\text{cm}^3}\right]$	7.24	7.11	6.98
ρ_{rel} [%]	98.6	96.89	95.1

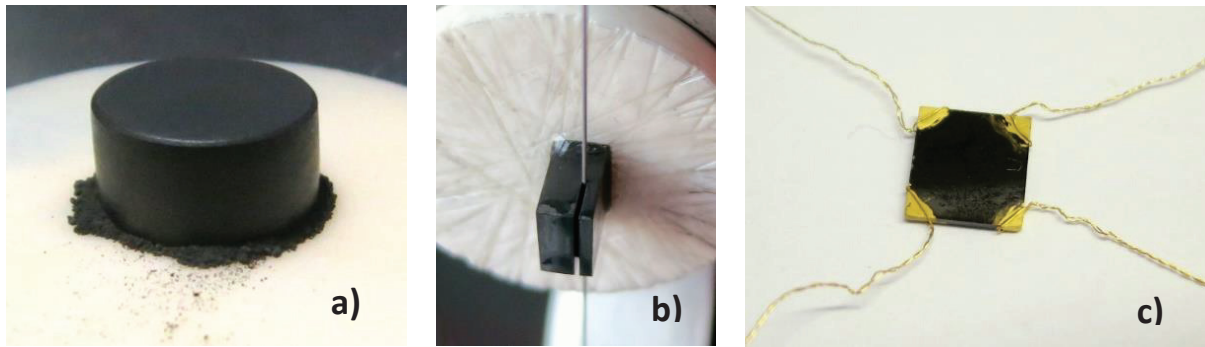


Figure 30: Sample preparation: a) sintered bulk sample, b) cutting process into thin rectangular slabs, c) contacted sample

Subsequently, the pellet was cut (Well - diamond wire saw) into thin rectangular slabs (Figure 30 b). One single slab was polished (Buehler Minimet Polisher) until plane parallel, highly polished surfaces and a constant thickness were obtained. Table 5 shows the geometric dimensions of the polished pellet.

Table 5: List of the polished pellets` dimensions
t... thickness of the sample, $l_1 / l_2...$ lateral length

	PNCO291_01 (decomposed)	PNCO291_02	PNO
l_1 [mm]	7.388	7.091	8.661
l_2 [mm]	6.789	7.457	7.435
t [mm]	0.703	0.562	0.493

The last working step was the contacting of the corners with gold according to van der Pauw (Figure 30 c) and the implementation into the quartz sample holder (Figure 31). To achieve this, four gold wires ($d= 0.1$ mm) were twisted and a loop was produced at their closed ends. These loops were attached to each corner of the sample using gold paste (Metalor T-10112). The paste was burned in for 15 min at 600°C (heating and cooling rate of 2K/min). It is necessary to keep the temperature below 700°C to avoid any phase decomposition process. Due to the fact that the thin gold wires deform upon heating, the position and the orientation (Figure 31) of the sample had to be fixed during measurements. For this purpose, the contacted sample was attached in a quartz sample holder. Connections between the sample holder and every wire were fortified with gold. Finally, the sample on the quartz holder was placed in the reactor and different measurements were performed.

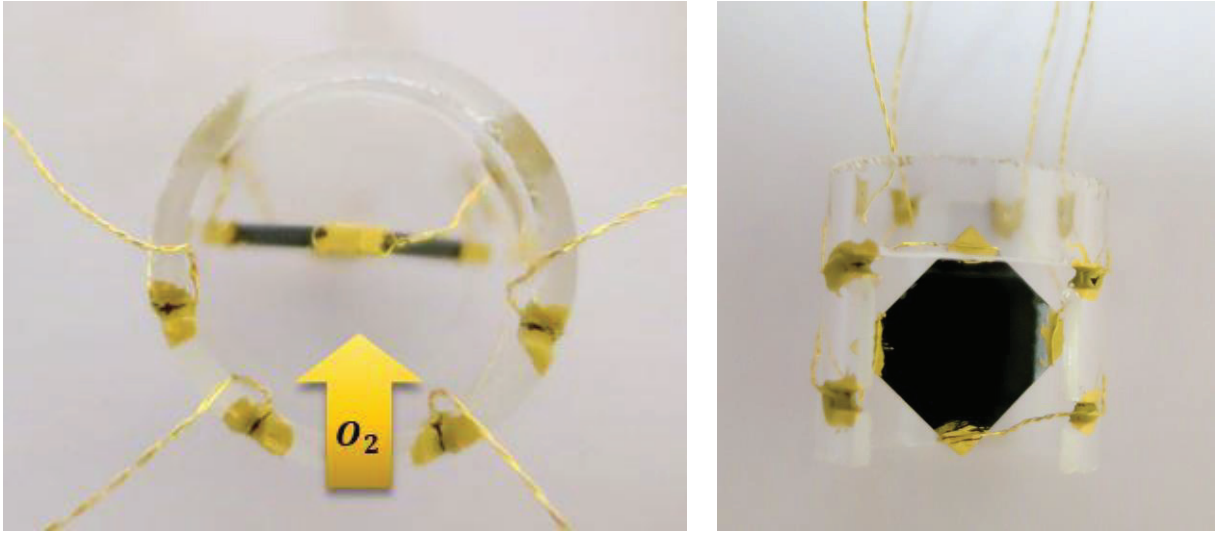


Figure 31: Contacted sample mounted in quartz holder. Sample mounted horizontally to ensure that diffusion takes place normal to the sample's surface

3. Characterization

3.1. Crystal Structure and Phase Composition

X-Ray diffraction of the powder and a subsequent analysis of the diffractogram through Rietveld method is a common way to identify the crystal structure and phase composition of the synthesized powder [39]. The measurement was performed at room temperature using a Bruker 8D Advanced with Cu-K α radiation. The XRD characterization of PNCO verified phase purity (Figure 32). According to that, 98% of weight fraction showed the K₂NiF₄ structure. Only a phase impurity of 2% could be indentified. It is assumed that here are no limiting effects on the functionality of the material, because the amount of second phases is very small.

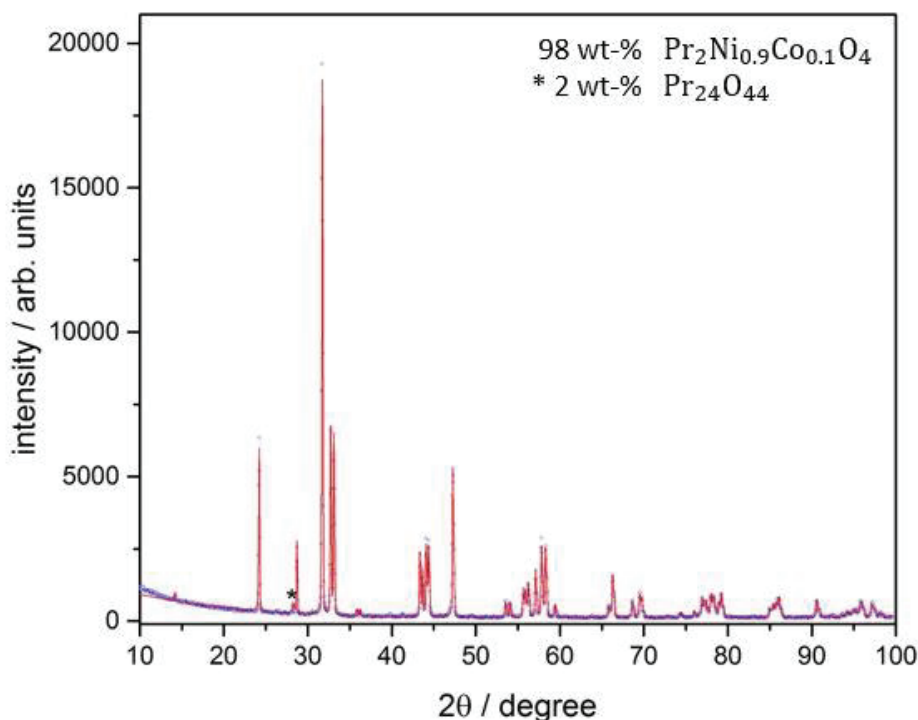


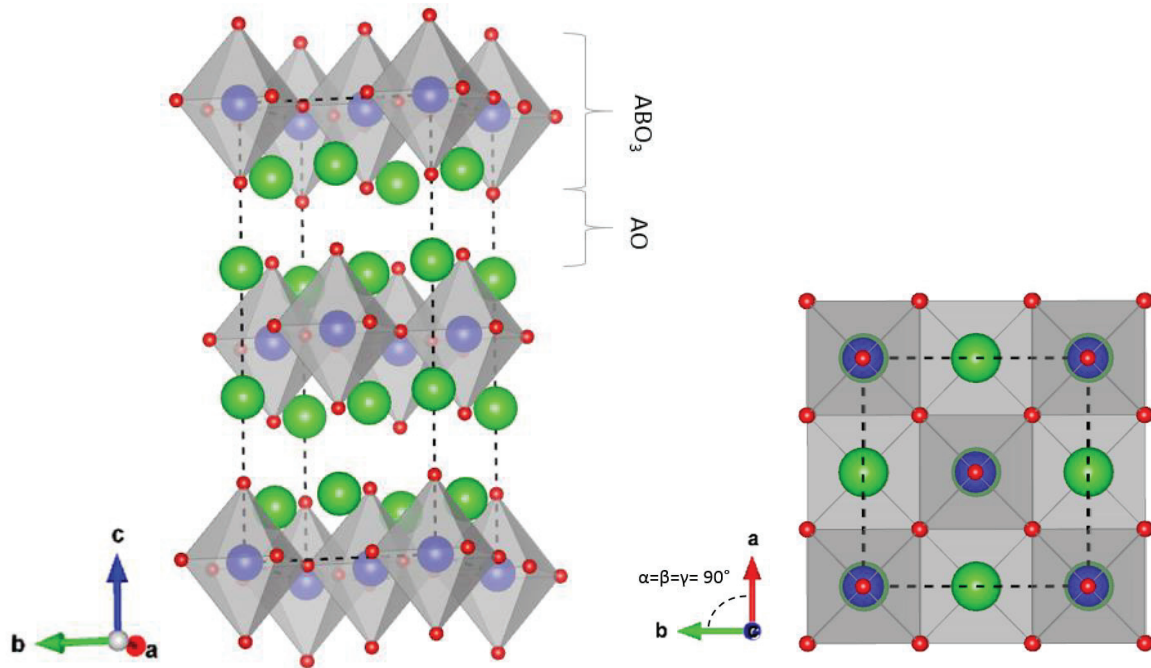
Figure 32: XRD-pattern of the investigated $Pr_2Ni_{0.9}Co_{0.1}O_{4+\delta}$

By using parameters of the diffractogram it is possible to determine following lattice parameters (Table 6). The R-value gives information about the deviation of the accuracy between the data from the crystallographic model and the experimental values from the X-ray diffraction. According to the result of 4%, the refined structure predicts the observed data very well.

Table 6: Lattice parameters of PNCO

cell length [Å]	cell angle [°]	cell volume [Å ³]	R value
a= 5.4594 b= 5.4086 c= 12.4078	$\alpha = \beta = \gamma = 90$	366.37	0.04072

Furthermore, the visualization of the crystal structure of PNCO (Figure 33) using the program Vesta was performed. The XRD proved that the material crystallizes in an orthorhombic structure (Fmmm), which was already reported for PNO [24, 40]. Due to the fact that only a small amount of cobalt was substituted to the material the assumption was made that PNCO behaves similarly to PNO.


 Figure 33: K_2NiF_4 -structure of PNCO showing unit cell (dashed line)

The illustration of the crystal structure is given by Figure 33. The lattice parameters confirm the K_2NiF_4 -structure consisting of the alternate layers of grey colored NiO_6 octahedra between layers of green colored A-site cations. The red colored oxygen anions are positioned at the vertices of NiO_6 octahedra, the blue colored B-site cations are located in the middle of the

octahedra. In the case of PNCO, the green spheres symbolize praseodymium-cations, the blue ones nickel and cobalt-cations. According to the diffractogram nickel and cobalt coexist next to each other.

3.2. Optimization of Sintering Program

A dilatometric analysis (Netzsch DIL 402 PC) was performed to find the optimal sintering temperature. The powder was heated up to 1350°C (heating and cooling rate 2K/min) and was being kept at this temperature for 10 hours. The shrinkage of the powder was recorded and is illustrated in Figure 34. It shows the change in length over time. The optimal sintering temperature was determined by fitting two tangents into the curve. According to that the calculated sintering temperature was 1120°C.

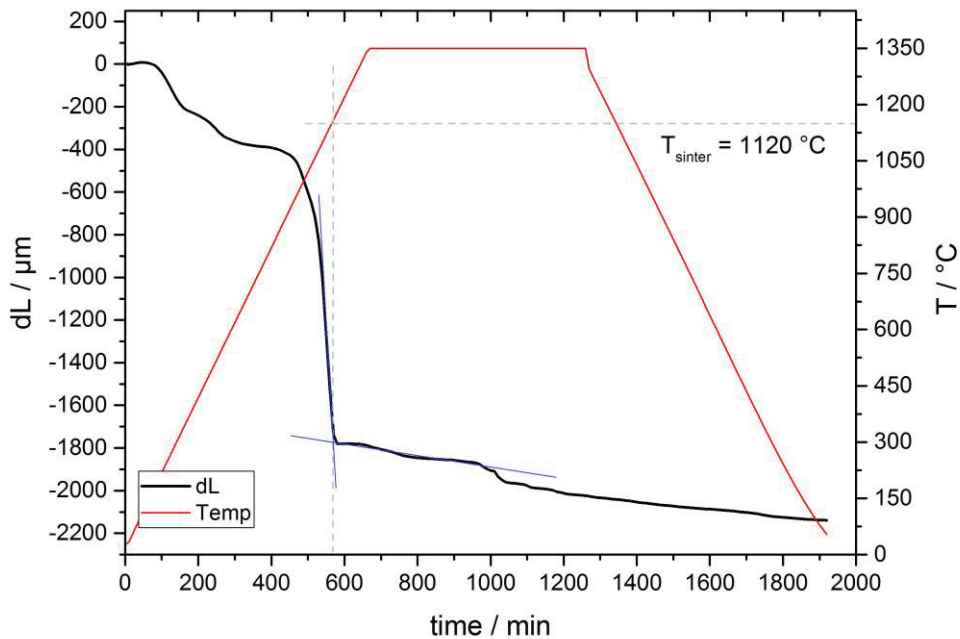


Figure 34: Dilatometric curve: length change over time

As a result, a pellet was sintered at 1120°C. The sintered bulk sample was investigated for possible phase transitions by XRD. The results are illustrated in

Figure 35 and Table 7. The top diagram presents the pattern of the single-phase powder after the freeze-drying process. The diagram at the bottom shows the diffractogram after sintering the bulk sample at 1120°C. Comparing the two charts, it is immediately clear that there are considerable changes. Some of the existing peaks have changed and in several places new peaks have been formed. This result is based on a transformation of PNCO to a higher Ruddlesden Popper phase. Consequently, the sintering temperature was wrongly established.

It was estimated that PNCO behaves like PNO, and thus it should have been stable at a sintering temperature of 1120°C. Therefore, following assumption was made: By adding a small amount of cobalt the instability region increases or changes. But how the region has changed remains an unanswered question. To solve this problem, additional measurements have to be performed to develop a phase diagram for PNCO.

Therefore, the sintering program was optimized. For further studies the sintering temperature was set at 1200°C. Finally, it was possible to produce a sintered single phase sample.

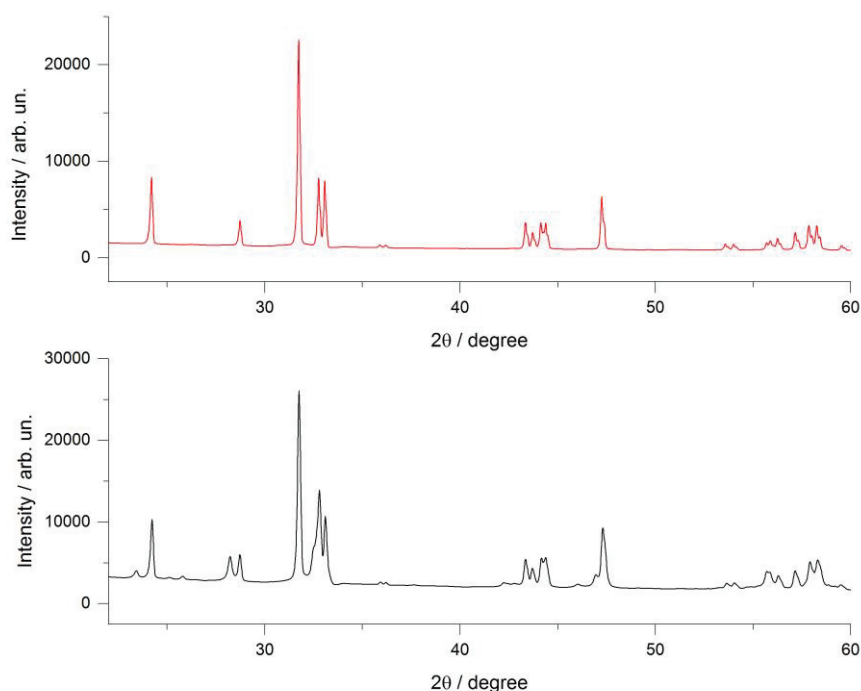


Figure 35: XRD patterns of the single phase PNCO powder (top) and decomposed PNCO sample (bottom)

Table 7: Phase composition of the decomposed sample sintered at 1120°C

Structure	Mass fraction [%]
Pr_2NiO_4	69
$\text{Pr}_4\text{Ni}_3\text{O}_{10}$	25
Pr_6O_{11}	6

3.3. Thermal Expansion Coefficient (TEC)

A dilatometric analysis (Netzsch DIL 402 PC) was performed in air between room temperature and 1000°C with the heating rate of 1°C/min. An Al₂O₃ standard was used for the calibration. Through linear regression it was possible to determine the thermal expansion coefficient. As shown in Figure 36, there are two distinct regions with differing gradients. Region one reaches from 30-400°C, region two from 400-1000°C.

Figure 36 shows the calculated thermal expansion coefficients at different oxygen partial pressures. The variation in slope is attributable to the reduction of Ni³⁺ to Ni²⁺. Precisely, it indicates the alteration from the orthorhombic to the high temperature tetragonal structure. However, the phase transition of PNCO to a higher Ruddlesden Popper phase, which occurs at around 750°C, cannot be indicated directly in the expansion curve.

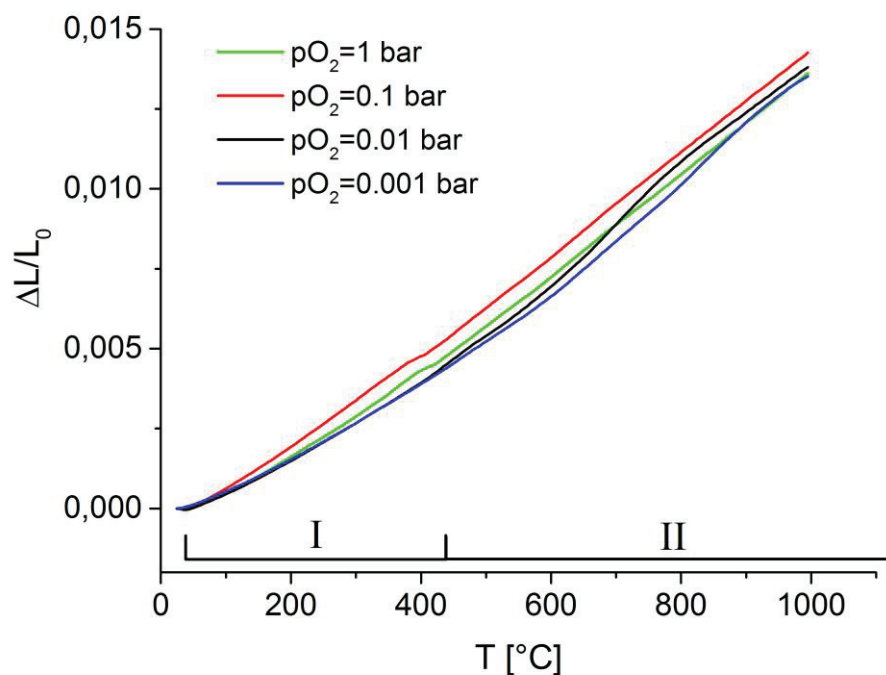


Figure 36: Thermal expansion in atmospheres with different oxygen partial pressure (heating rate: 1°C/min)

Table 8: Thermal expansion coefficient with a heating rate of 1K/min at different oxygen partial pressure p_{O_2}

p_{O_2} [bar]	α (30 - 400°C) [10^{-6} K^{-1}]	α (400 - 1000°C) [10^{-6} K^{-1}]
10^{-3}	10.82	16.87
10^{-2}	11.19	16.06
0.1	13.75	16.19
1	12.23	15.89

Previous studies have already shown that materials substituted with cobalt usually exhibit a higher thermal expansion than others [16-18, 41, 42]. For example: The thermal expansion coefficient of $\text{La}_2\text{NiO}_{4+\delta}$ is $\alpha = 13 \times 10^{-6} \frac{1}{\text{K}}$ [17]. By substituting the B-site cation with cobalt, $\text{La}_2\text{Ni}_{0.9}\text{Co}_{0.1}\text{O}_{4+\delta}$, the value increases. In that case, α is $14.2 \times 10^{-6} \frac{1}{\text{K}}$ [42]. According to A. Egger [1] the thermal expansion coefficient for $\text{Pr}_2\text{NiO}_{4+\delta}$ is $15 \times 10^{-6} \frac{1}{\text{K}}$. The experiment has repeatedly confirmed, that the thermal expansion coefficient increases due to the fact that cobalt was substituted to the material.

As mentioned before, the matching of thermal expansion coefficients between electrode materials and electrolytes is necessary to avoid delamination effects [3, 10]. Thus, the thermal expansion coefficients for PNCO are slightly higher (23%) than those of common electrolytes such as yttria-stabilized zirconia (8 mol% YSZ) or gadolinia-doped ceria ($\text{Ce}_{0.9}\text{Gd}_{0.1}\text{O}_2$). Both materials have thermal expansion coefficients in the range between $10 \times 10^{-6} \frac{1}{\text{K}}$ and $13 \times 10^{-6} \frac{1}{\text{K}}$. However, the results are close to the required $\pm 20\%$ range [43, 44].

3.4. Thermogravimetric Analysis

The experiment (equipment: thermobalance Setaram TAG 16) was performed under oxidizing conditions (20% O₂, rest Ar). The sample was heated up to 900°C (maintained for two hours) with a 5 K/min heating and cooling rate.

According to Figure 37 the first major mass loss occurs around 400°C. It shows an agreement with the TEC-results: a reversible structural change from orthorhombic to tetragonal lattice. The main transition can be indicated at around 750°C. The irreversible mass increase is caused due to the fact that the material takes up oxygen during every cycle. Nevertheless, the results also indicate that PNCO stabilizes quickly, because with every cycle the mass increase decreases.

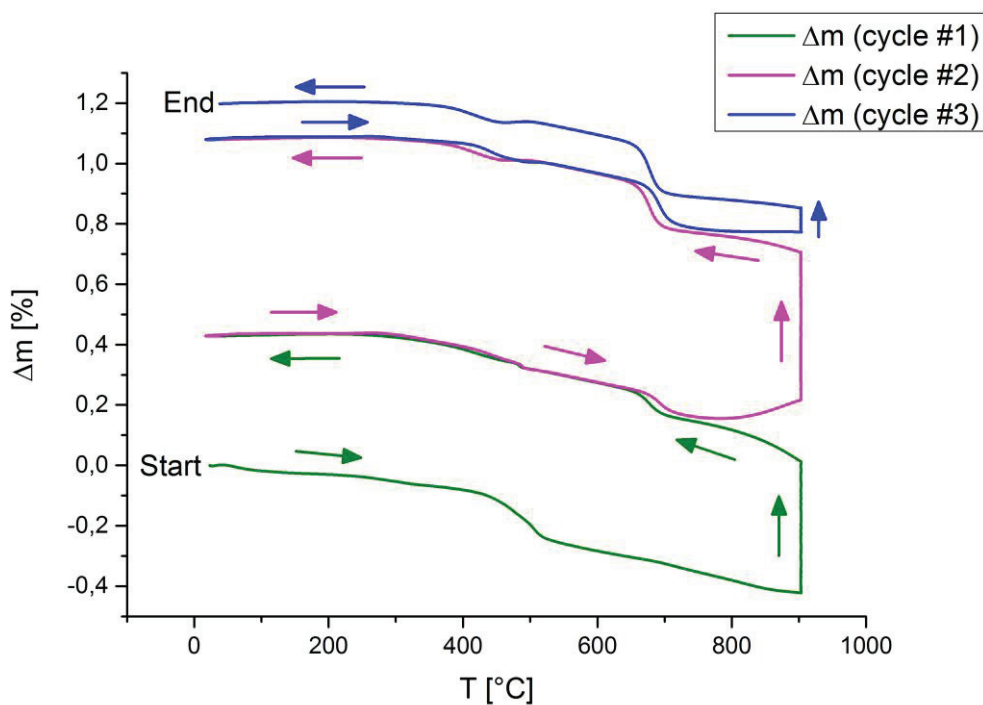


Figure 37: TG curve of PNCO, measurement performed in 20% O₂, rest Ar

For comparison, the TG-measurement was repeated for PNO. The experiment was carried out under same conditions. Figure 38 shows the TG curve of PNO. The chart indicates that the process of phase transition has already been completed in the third thermal cycle (blue line).

In that case, the curve progression is almost reversible. Thermal hysteresis effects cause the deviation of the heating up and cooling down progression of the blue curve. Nevertheless, the system maintains in a thermodynamical equilibrium (all further measurements would show a similar curve). Consequently, there will be no mass increase at 900°C anymore because the material does not take up any further oxygen.

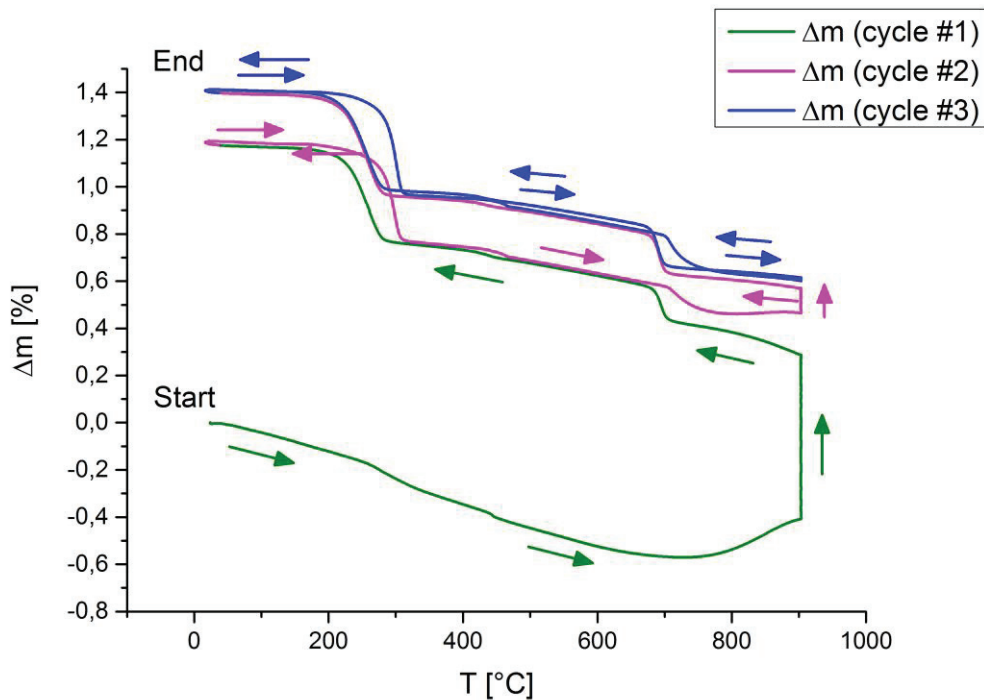


Figure 38 : TG curve of PNO, measurement performed in 20% O₂, rest Ar

Comparing the TG curves of PNCO and PNO, both charts indicate a continuous oxygen release upon further heating around 400°C. Furthermore, a significant mass increase can be indicated in both illustrations at around 750°C. The decomposition rates of both materials decrease in each subsequent TG-run. The only difference is the width of the curves in every cycle, which is an indicator for the decomposition rate. The higher the value of the curve's width the more intense the transition to a higher Ruddlesden Popper phase takes place. However, PNO gets into balance more quickly. As mentioned in Chapter 1.6.2, in pure argon no mass increase is visible at high temperatures.

For the purpose of further analyzing the decomposition of the acetate precursor of PNCO, TG measurements were performed in inert and oxidizing conditions (Figure 39). As expected, there is no sign of any mass increase during cooling in argon (blue curve). The result in 20 % O₂ does not show a reversible curve progression. This effect occurs due to the pronounced mass loss during the decomposition of the precursor (approx. 50%) and the comparatively small uptake of oxygen of the formed oxide PNCO during cooling (approx. 0.4%, see Figure 37).

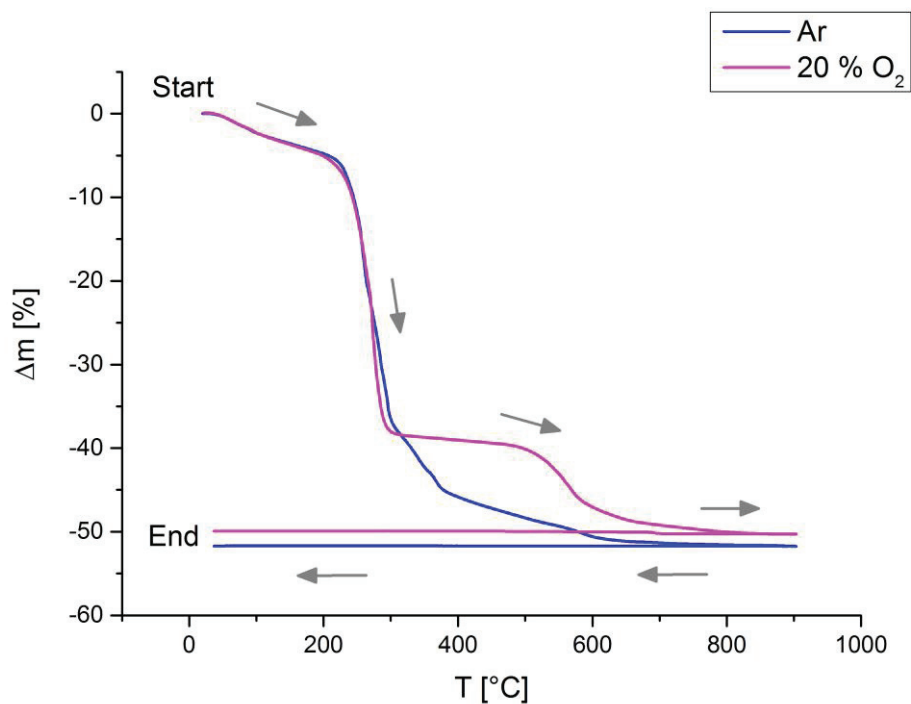


Figure 39: Decomposition of the acetate precursor of PNCO, TG measurements performed in inert (100% argon) and oxidizing (20% O₂, rest Ar) conditions

3.5. Differential Scanning Calorimetry

The experiment (equipment: Netzsch DSC 404 PC) was performed under inert conditions (pure argon). The sample was heated up to 1000°C with a 20 K/min heating and cooling rate. Since oxygen exchange only occurred during the heating, only the result of the heating up was interpreted.

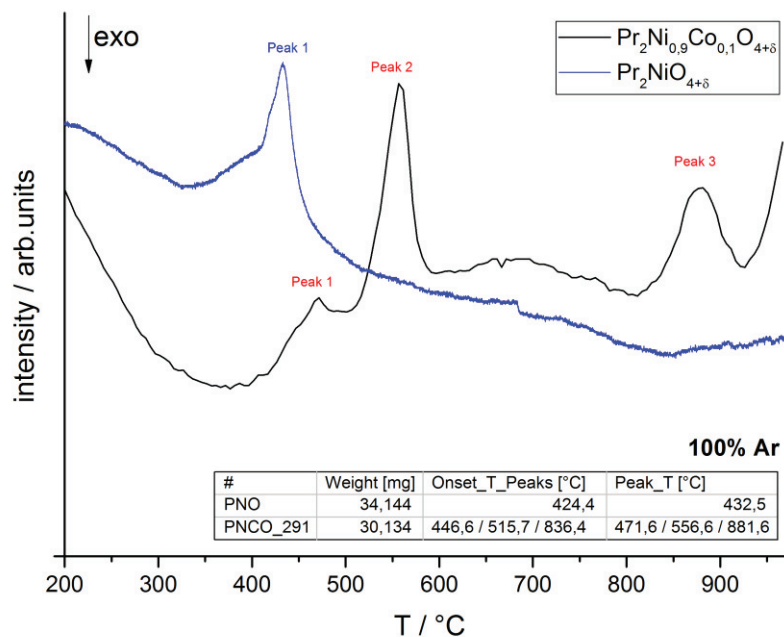


Figure 40: Comparison of DSC curves of PNO and PNCO, measurement performed in pure argon

Again, the previously presented results (TG, TEC) can be reproduced, a first indicator for the first order phase transition takes place at 450 to 560°C (structural change from low temperature orthorhombic to high temperature tetragonal). The same observation was made for PNO (blue curve), where the structural change occurs at 420°C.

As mentioned in Chapter 1.6.3, the peaks in the DSC curves can either be exothermic or endothermic, depending on whether the sample is heated up or cooled down. During the heating process oxygen gets released, this leads to an endothermic peak as expected. Due to the fact that the measurement was performed in pure argon, no peaks were found during the cooling down process. This is expected because there is no oxygen available in the surrounding

atmosphere. However, a broad endothermic peak in the black colored DSC-curve of PNCO can be observed between 830 and 900°C, which exactly indicates the phase decomposition to the high temperature Ruddlesden Popper phase. The result of the DSC measurement disagrees slightly with the one of the TG experiment due to the difference in their heating and cooling rate.

The measurement of PNO but also of PNCO was repeated in an atmosphere consisting of 20 % oxygen, rest argon. The DSC-plots show the first order reversible phase transition (Figure 41). An additional peak at 500°C distinguishes the cobalt substituted material from the Co-free PNO (main difference to the measurements performed in Ar). This phase transition is caused by slight changes of the unit cell.

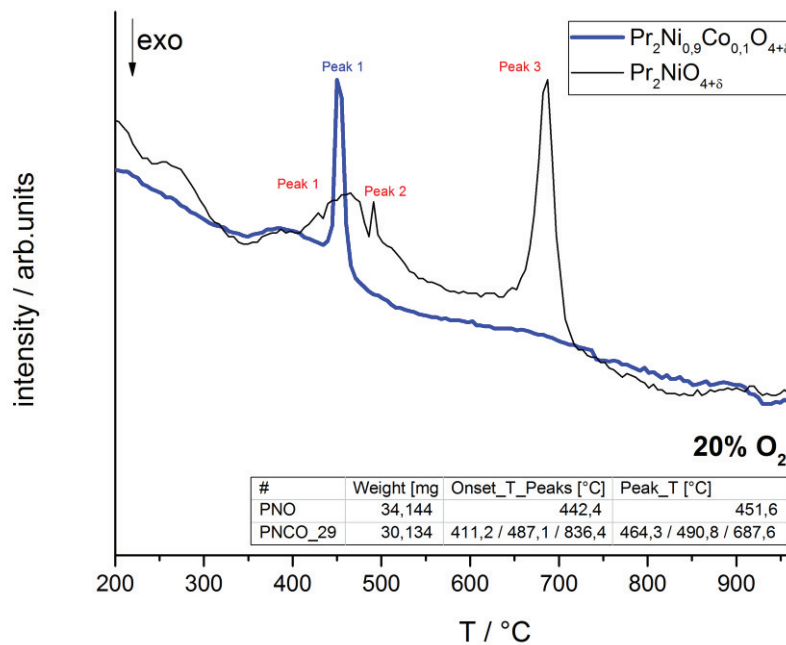


Figure 41: Comparison of DSC curves of PNO and PNCO, measurement performed in 20% O₂

Figure 42 and 43 show the whole DSC-result during heating and cooling performed in Ar and 20% O₂. Big differences in curve progression can be observed upon cooling. Due to the absence of oxygen, no further peaks are visible in pure Ar, as expected. On the contrary, for PNO the pink curve indicates a major exothermic peak at around 700°C due to the uptake of oxygen.

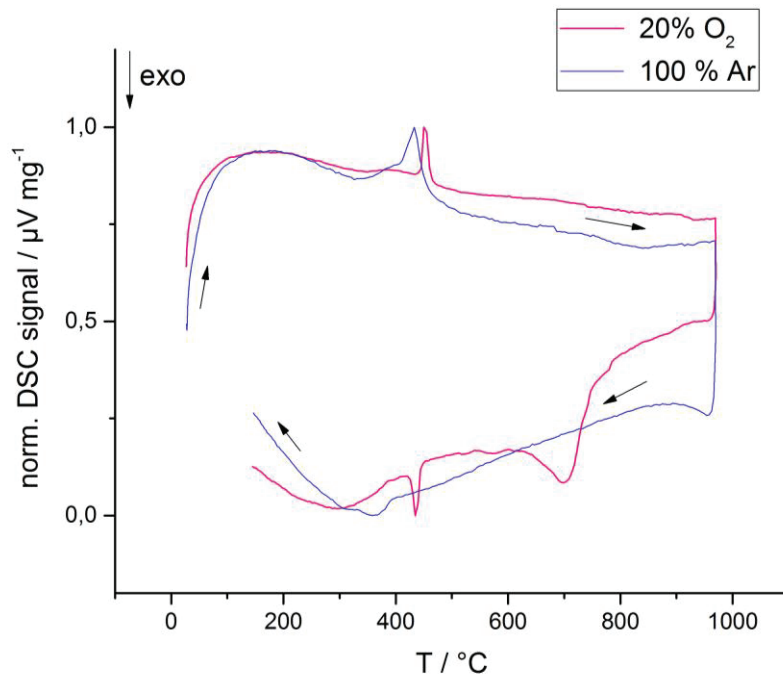


Figure 42: Comparison of the DSC curves of PNO performed in argon (blue) and 20% O₂, rest Ar (pink)

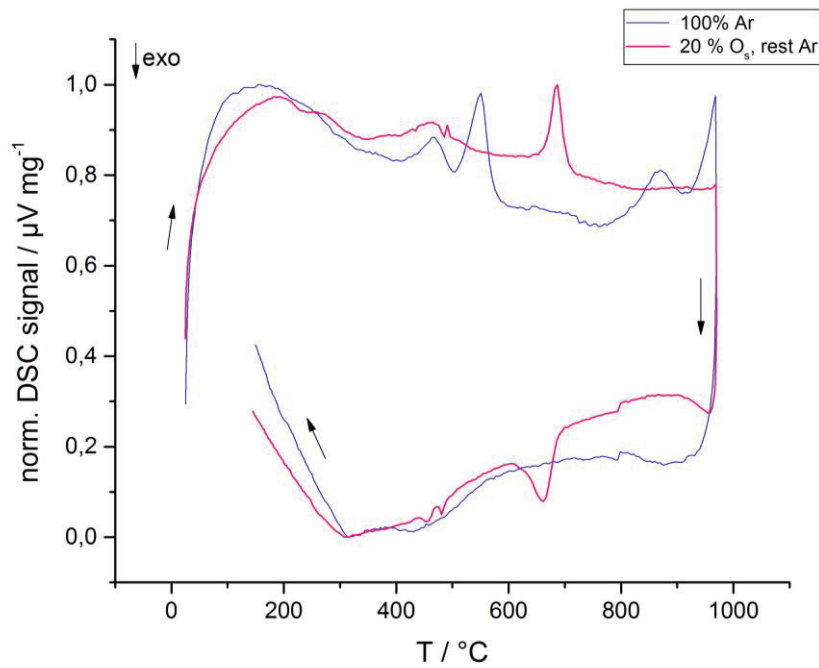


Figure 43: Comparison of the DSC curves of PNCO, performed in argon (blue) and 20% O₂, rest Ar (pink)

However, a small visible deviation exists between the two individual curves. By adding O₂ to a system in equilibrium at constant volume, the partial pressure will increase. As the curve

indicate, the oxygen partial pressure increase leads to a shifting of the phase transition (shift of the base line) to lower temperatures, which has been already reported for PNO [1, 7]. The same effect can be observed for PNCO.

3.6. Mass and Charge Transport Properties

A phase-pure dense PNCO pellet was used for studies of the oxygen exchange kinetics by the dc-conductivity relaxation method. The results will be discussed in following chapters. Due to the fact that the behavior of PNCO has never been reported in detail in previous studies, a preliminary study was performed. As mentioned in Chapter 1.3, a decomposed pellet (wrongly established sintering temperature) was produced. For test purposes, the bulk sample was prepared according to the Van der Pauw method and investigated with respect to its transport properties as a function of temperature and oxygen partial pressure. The same experiment was repeated for PNO to make a comparison between the results more meaningful.

3.6.1. Experimental Setup

After implementing the sample into the reactor the electronic conductivity measurements and the conductivity relaxation measurements can be performed. The setup used for both measurements is shown in Figure 44. The quartz reactor was placed in a horizontal tube furnace. During the whole experiment, the temperature was adjusted through a Eurotherm Mod. 2604 temperature controller (operating range during the experiment 700-800°C). In order to prevent phase decomposition of PNCO into a higher Ruddlesden Popper phase, experiments are performed in a controlled atmosphere with a high argon content and a low oxygen content. The flow rate was fixed at 2L/h. The oxygen partial pressure (pO_2) and temperatures in the reactor were recorded with a potentiometric sensor (integrated S-thermocouple). Due to the fact that the reactor shows a small temperature gradient along its length, the sensor was placed in the direct vicinity of the sample. The sensor signal was measured with a high impedance voltmeter (Keithley Mod. 2000). In both experiments the currents were applied using a source-meter (Keithley Mod. 2400), which possesses the ability to act as current source or a voltmeter. During the conductivity relaxation measurement the voltage was measured with a nano-voltmeter (Keithley Mod. 2182). To enable a manual switching between the different gas streams a four way valve was used [1].

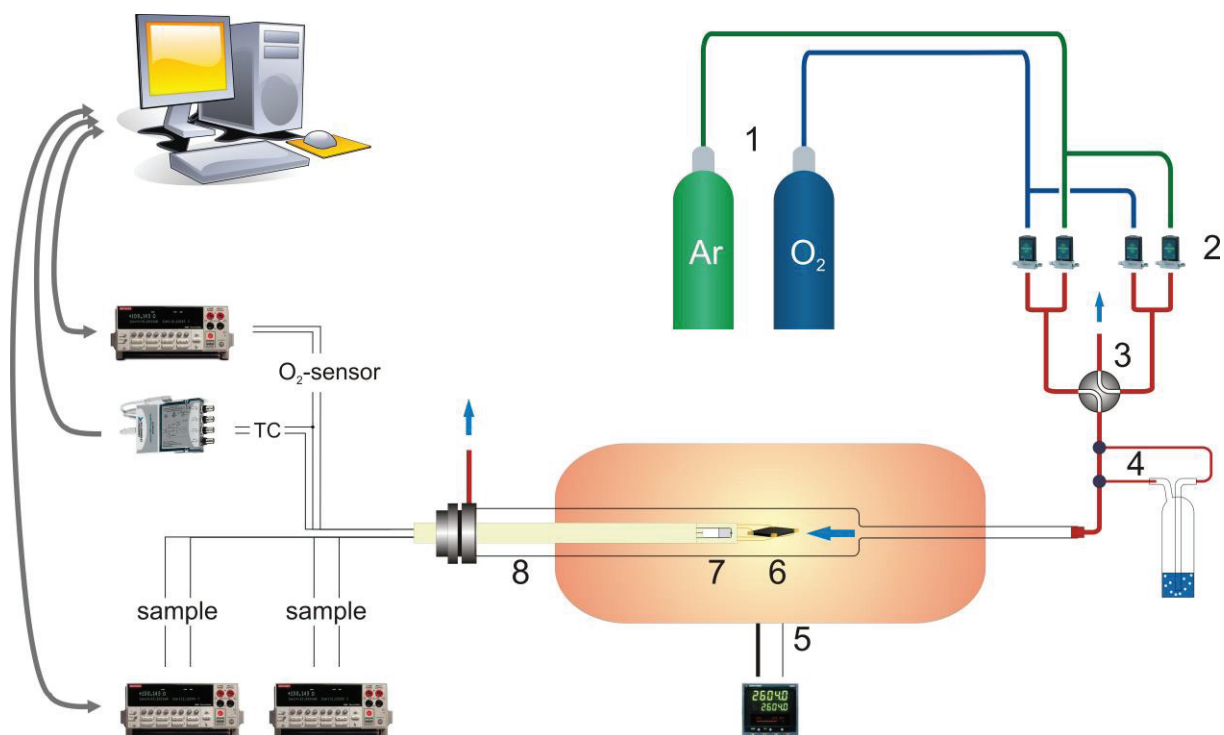


Figure 44: Setup for conductivity and conductivity relaxation measurements [1]

1... gas supply (mixture of O₂ and Ar), 2... mass flow controller, 3... manual four-way valve, 4... humidifier (only used for degradation investigations), 5... temperature controller, 6... examined bulk sample, 7... oxygen sensor (integrated thermocouple), 8... reactor/sample holder/flange, blue arrows symbolize direction of the gas flow

All measurements for the determination of the transport properties of PNCO were performed in oxygen reduced atmosphere (1.0×10^{-3} bar p_{O_2} or 1.5×10^{-3} bar p_{O_2}) to avoid further phase decompositions due to the instability of the material. The experiments were executed at temperatures between 600 – 800°C in 50°C steps.

3.6.2. Electronic Conductivity Measurement (σ)

The electronic conductivity (σ) was determined. A current of 100 mA was applied. The result (Figure 45, blue curve) indicates that the conductivity increases for higher pO_2 values. The reduction reaction takes place at low pO_2 because of a compensation through releasing oxygen, which leads to the decrease in conductivity. Furthermore, it can be observed that the conductivity decreases with the increase in temperature. During heating the charge carrier mobility (migrating electron holes located on nickel ions) gets limited while the charge carrier amount remains constant. This leads to a decrease in conductivity [45, 46]. This effect is heightened due to a further transition of the material to higher Ruddlesden Popper phases (temperatures higher than 750°C). This exactly confirms the outcome of previous researches (TG, DSC).

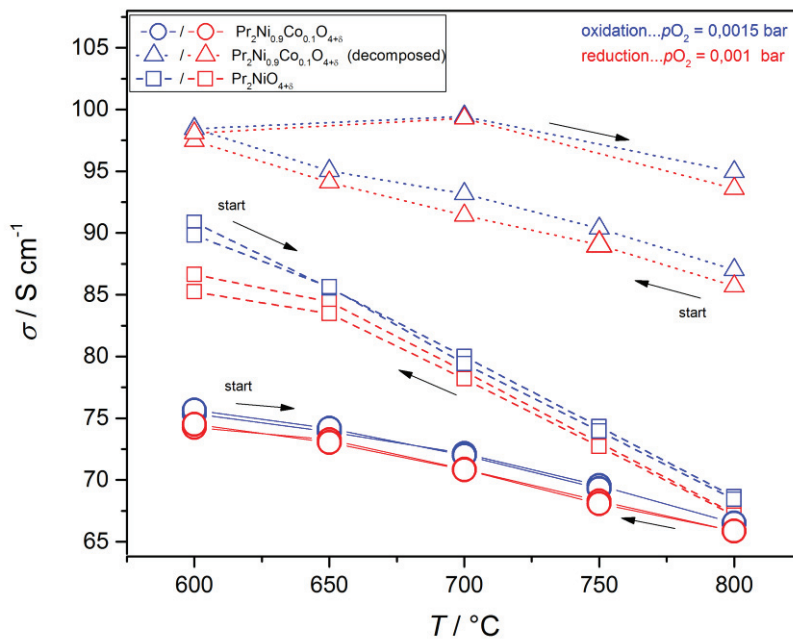


Figure 45: Relation between electronic conductivity and temperature of phase pure PNCO, the decomposed PNCO sample and PNO. Results obtained from oxidation and reduction steps are colored blue and red, respectively

Higher Ruddlesden Popper phases $A_{n+1}B_nO_{3n+1}$ ($A = \text{Pr}$; $B = \text{Ni, Co}$; $n > 1$) are known to have higher electrical conductivities. Usually, the conductivity increases with n due to the increasing incidence of B-O-B interactions in the perovskite layers (enhancement of electronic conduction pathways) [47]. This effect can be confirmed by performing the experiment using the decomposed sample (consisting of 30% secondary phases, including the 3rd order Ruddlesden Popper phase). As can be seen in Figure 48, the value of σ at the beginning of the measurement is much higher than the one of the phase pure sample. In addition to that, this effect is heightened during the measurement. A further transition and hence an increase of σ takes place in every measurement cycle. The same effect was confirmed for $\text{La}_2\text{NiO}_{4+\delta}$ and for its higher order Ruddlesden-Popper phase $\text{La}_4\text{Ni}_3\text{O}_{4+\delta}$ by Amow and Skinner [48]. For $\text{La}_4\text{Ni}_3\text{O}_{10+\delta}$ the values for the electrical conductivity are higher than those for $\text{La}_2\text{NiO}_{4+\delta}$.

Comparing the result of the phase-pure PNCO sample with PNO the value of σ decreases by 10 percent at all temperatures. In this context, the circumstance that the substitution with cobalt would improve the electronic conductivity did not occur. The exact reverse is the case. The presumable cause of the decrease is the change in the stoichiometry due to the substitution with cobalt, which leads to an enhancement of the ionic conductivity due to the formation of vacancies. Therefore, the rising concentration of vacancies results in a decrease of the electronic conductivity. To proof this effect, the ionic conductivity has to be determined for PNCO through additional measurements. The comparison of the ionic and electronic conductivity will validate the hypothesis. There are different studies that already proved the decrease of the conductivity due to the presence of cobalt. A study by Nomura, Nishimoto [49] investigated the electrical conductivity of PNCO for low temperatures. They showed that the conductivity is lower due to the presence of cobalt (Figure 47). According to Amow [48] the system of $\text{La}_2\text{Ni}_{1-x}\text{Co}_x\text{O}_{4+\delta}$ tends toward insulating behavior by introducing cobalt (Figure 46). The higher the cobalt content in the tetragonal phases ($x=0.1$ to ~ 0.7), the greater the Ni(Co)-O bond length, which results in a decrease of the Ni(Co)-O covalent interactions

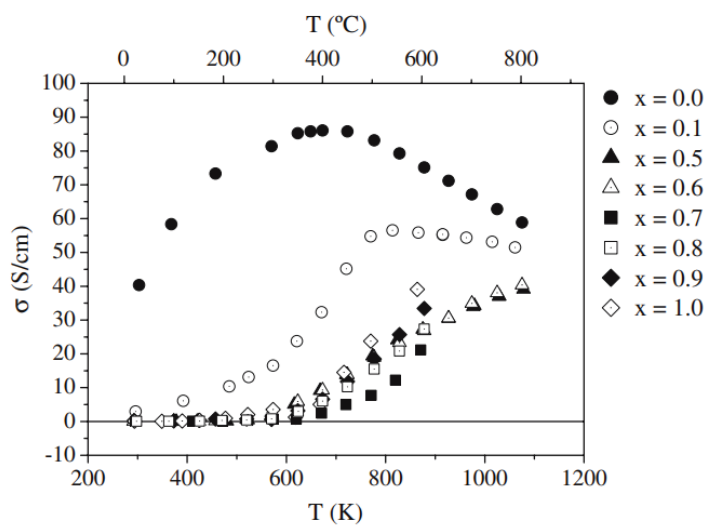


Figure 46: Electrical conductivity σ for $\text{La}_2\text{Ni}_{1-x}\text{Co}_x\text{NiO}_{4+6}$ according to Amow [48]

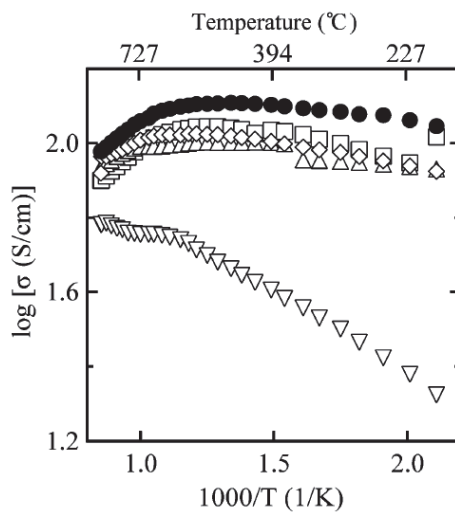


Figure 47: Electrical conductivity for Pr_2NiO_4 (circles), $\text{Pr}_2\text{Ni}_{0.9}\text{Cu}_{0.1}\text{O}_4$ (triangles), $\text{Pr}_2\text{Ni}_{0.75}\text{Cu}_{0.25}\text{O}_4$ (squares), $\text{Pr}_{1.91}\text{Ni}_{0.71}\text{Cu}_{0.24}\text{Ga}_{0.05}\text{O}_4$ (diamonds), and $\text{Pr}_2\text{Ni}_{0.9}\text{Co}_{0.1}\text{O}_4$ (inverted triangles)[49].

3.6.3. Chemical Surface Exchange Coefficient (k_{chem})

The surface exchange coefficient of a bar-shaped sample with linear four-point electrode arrangement was determined as shown in Figure 48 and 49. The values for k_{chem} are higher when changing from the lower to the higher $p\text{O}_2$ level (oxidation, blue line in the diagram) due to the fact that during oxidation process the surface exchange takes place faster than during reduction one (red line in the diagram). Additionally, it can be seen that k_{chem} increases with the increase in temperature. The value of k_{chem} of the phase pure sample is in the range of $10^{-4} \frac{\text{cm}}{\text{s}}$ (low temperatures) to $10^{-5} \frac{\text{cm}}{\text{s}}$ (high temperatures). It needs to be mentioned that the decomposed sample was measured from high temperatures to the low ones and back.

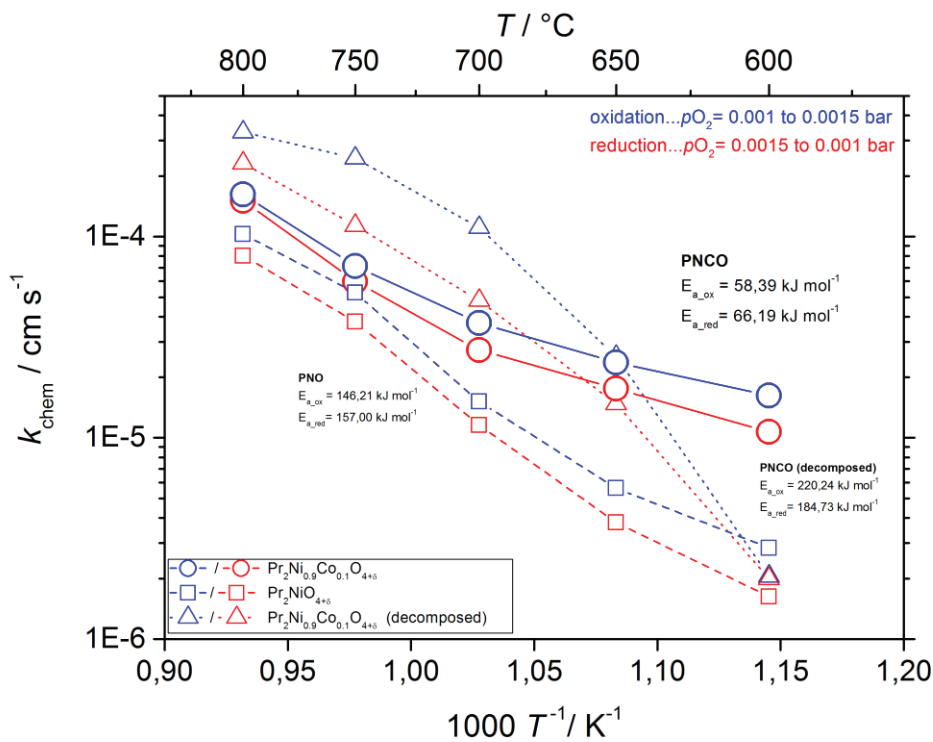


Figure 48: Relation between surface exchange coefficient k_{chem} and temperature of phase pure PNCO, the decomposed PNCO sample and PNO during heating up (600-800 $^{\circ}\text{C}$, 50 $^{\circ}\text{C}$ steps). Results obtained from oxidation and reduction steps are colored blue and red, respectively.

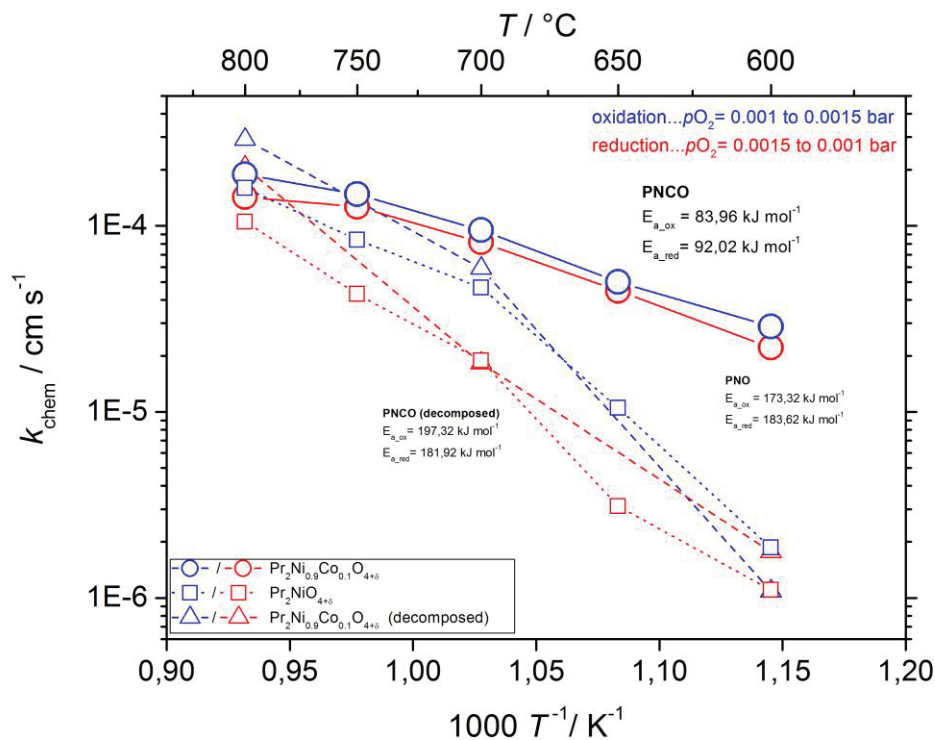


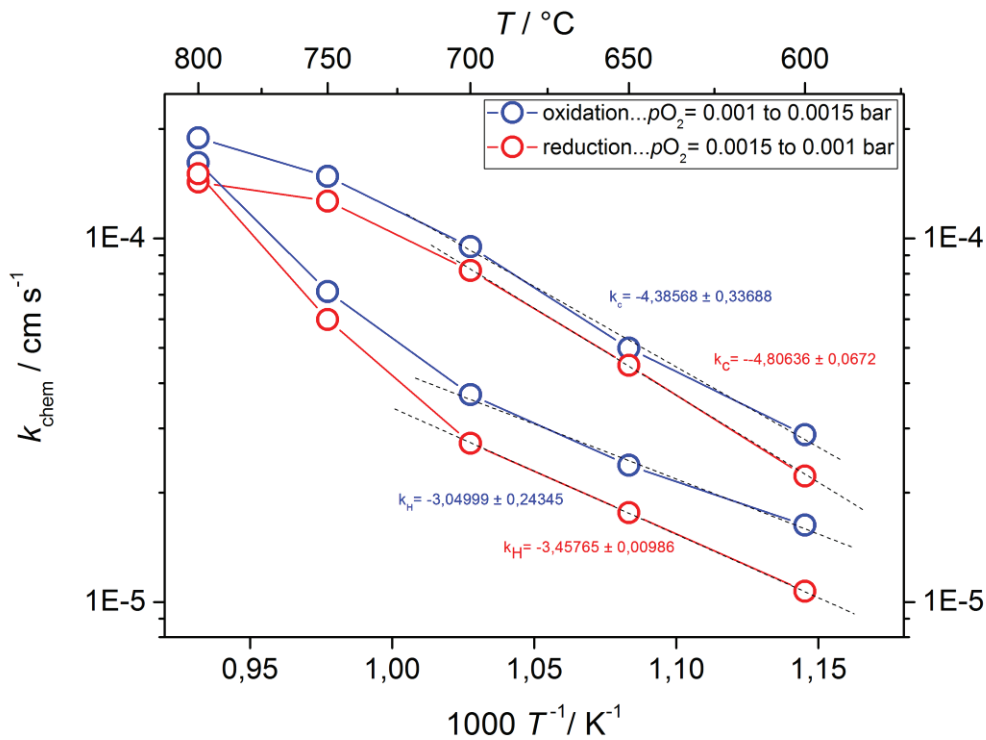
Figure 49: Relation between surface exchange coefficient k_{chem} and temperature of phase pure PNCO, the decomposed PNCO sample and PNO during cooling down (800-600°C, 50°C steps). Results obtained from oxidation and reduction steps are colored blue and red, respectively.

Comparing the result of PNCO with the result of the measurement of PNO the calculated k_{chem} -values of PNCO are the power of ten higher than those reported for PNO at low temperatures. In general, the enhancement of k_{chem} is attributable to both the increase in the number of oxygen interstitials due to the increase of δ , and the decrease of the rare-earth cation size ($\text{La} > \text{Pr} > \text{Nd}$). Thus, k_{chem} increases due to the substitution of the B-site with higher valence cobalt ions [15, 18].

Surprisingly, considerable changes in the shift in the slope of the k_{chem} -curve can be observed (Figure 50). Therefore, the resulting calculated activation energies E_a (see Table 9) are significant lower for PNCO. The values of E_a are roughly one third of that of the Co-free PNO.

Table 9: Activation energies E_a of k_{chem} calculated from the slope of the Arrhenius plot by linear regression ($T=600-700^\circ\text{C}$)

#	Mode	Reaction	slope	E_a [$\frac{\text{kJ}}{\text{mol}}$]
PNCO291_01 (decomposed)	cooling	reduction	-9.503	181.92
PNCO291_01 (decomposed)	heating	reduction	-9.649	184.73
PNCO291_01 (decomposed)	cooling	oxidation	-10.307	197.32
PNCO291_01 (decomposed)	heating	oxidation	-11.504	220.24
PNO	cooling	reduction	-9.591	183.62
PNO	heating	reduction	-8.200	157.00
PNO	cooling	oxidation	-9.053	173.32
PNO	heating	oxidation	-7.637	146.21
PNCO291_02	cooling	reduction	-4.806	92.02
PNCO291_02	heating	reduction	-3.458	66.19
PNCO291_02	cooling	oxidation	-4.386	83.96
PNCO291_02	heating	oxidation	-3.050	58.39


 Figure 50: Determination of E_a through linear regression

As shown in Figure 50, the results indicate that during the decomposition processes the slope gets altered. The curve can be separated into two parts. The slope of the regression curve at temperatures up to 700°C is smaller compared to high temperatures ($750 - 800^\circ\text{C}$). This once

again confirms the instability of PNCO. All in all, the presence of the transition metal Co in the K_2NiF_4 structure has a significant impact on the surface properties. But the origin of this effect cannot be identified so far. Further investigations are necessary to proof its evidence.

3.7. Surface Analysis

To check the surface of PNCO for any visible second phases, a small piece of the sample was polished and investigated through a scanning electron microscope (SEM). The composition of the material was obtained through Energy Dispersive X-ray analysis (EDX). The result can be seen in Figure 51. On the polished surface no second phases could be found. The structure contains a high amount of Pr, Ni and O, which was expected. It was not possible to obtain any Co within the structure through EDX.

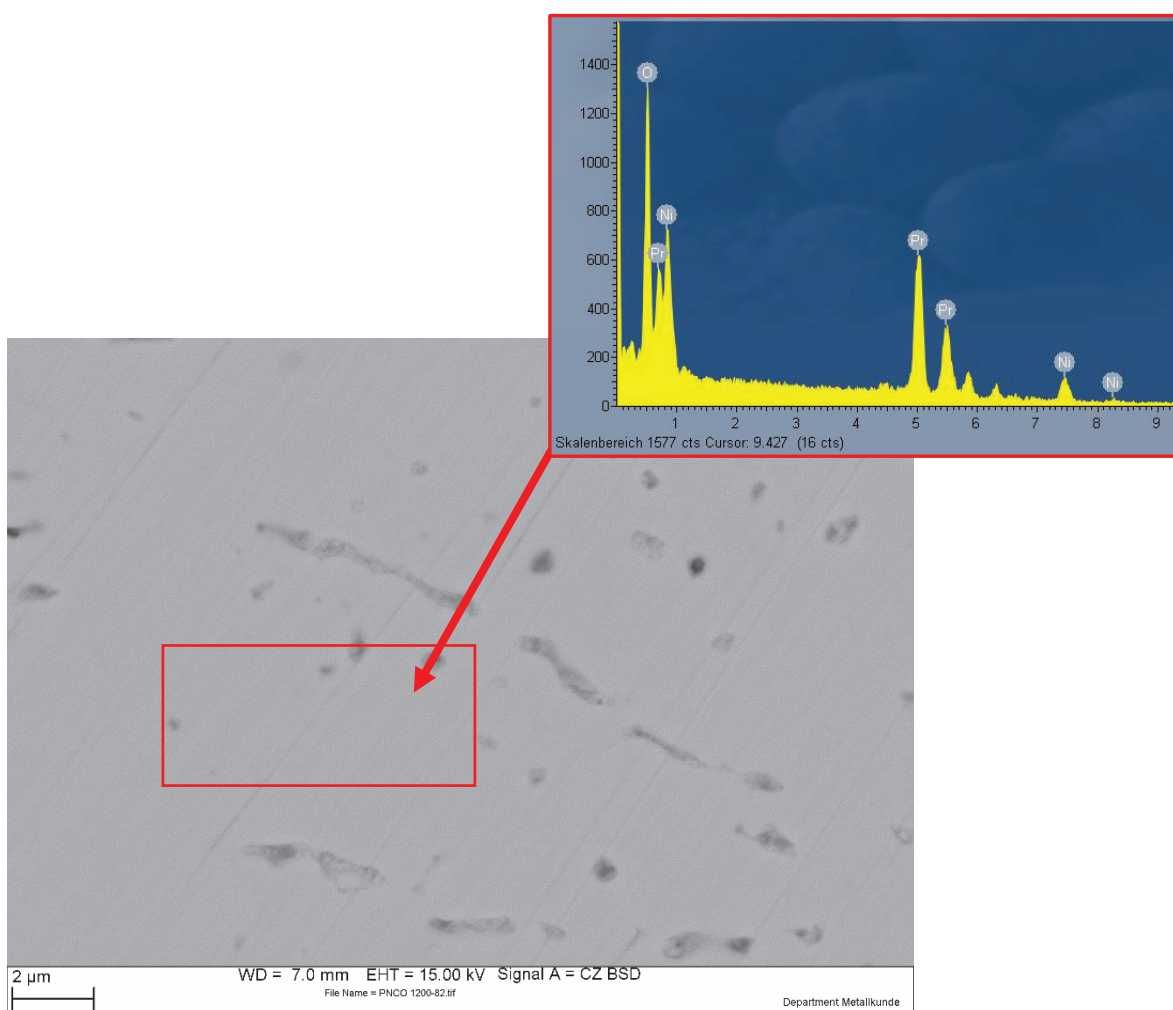


Figure 51: SEM image of the polished surface of PNCO and EDX spectrum from the region marked in red, black spots in the SEM image represent pores within the material

To obtain the grain size of the structure, a polished pellet was thermally etched. Generally, oxide ceramics are thermally etched in air. For this purpose a polished sample is placed in an oven. Temperature and time are selected in a way that the heat treatment does not lead to a change in the microstructure. During the etch process oxide layers are formed at the grain boundaries. Usually, the temperature should be 50°C below the sintering temperature. A wrongly established etching-program may result in heavy grain growth [50]. Due to the instability of PNCO the etching temperature was identical to the sintering temperature. The pellet was heated up to 1200°C with a 10 K/min heating and cooling rate. At temperatures around 1150°C a phase transition already occurs. The result can be seen in Figure 52.

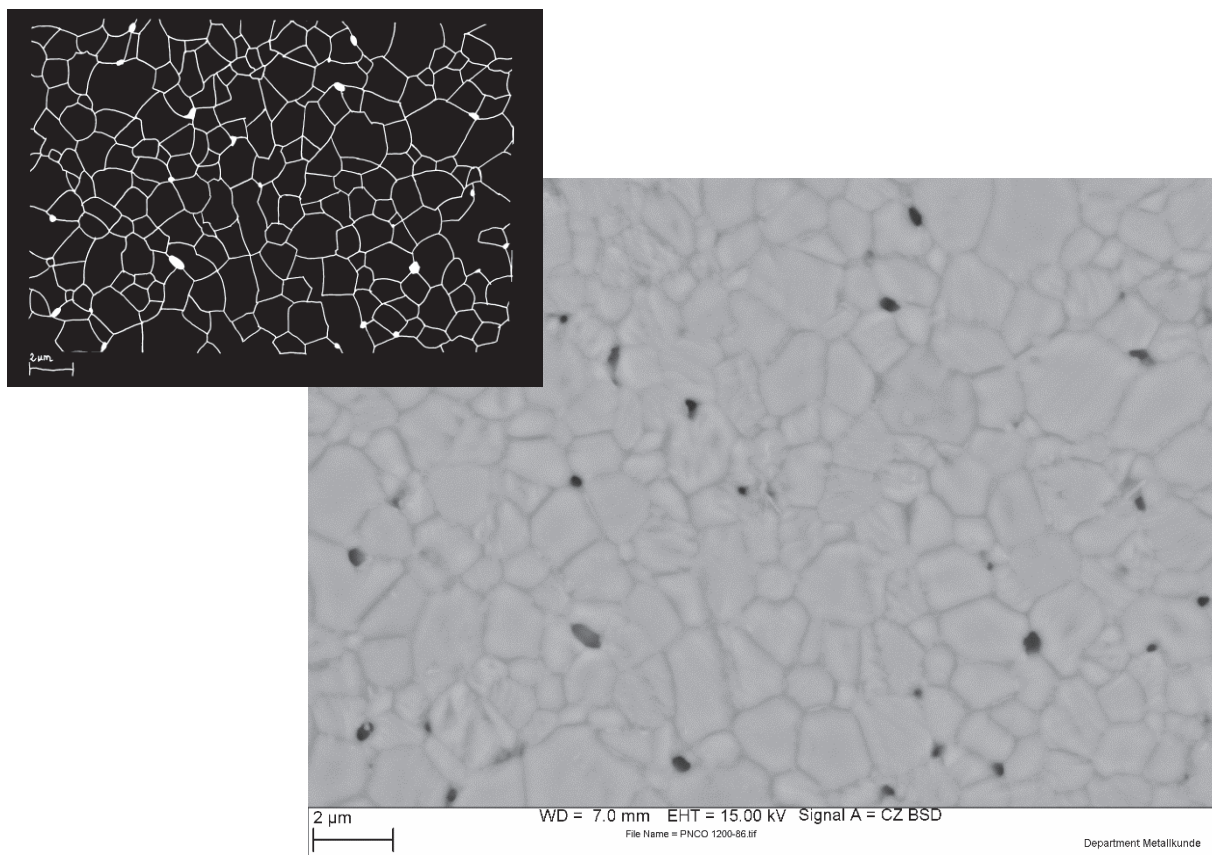


Figure 52: SEM of the etched sample (1200°C, 10 K/min heating and cooling rate)

By using the program ImageJ the average grain size was obtained. Before the SEM-image was ready for analyzing, the contrast between particles and background was highlighted (differences in the shades of grey) as shown in Figure 52. By using an algorithm, provided by the program, it was possible to calculate the Feret's diameter of the material's particles. The Feret's diameter can be defined as the average distance between pairs of two parallel planes to the outline of the particle [51]. The result of the average particle size is shown in Figure 53.

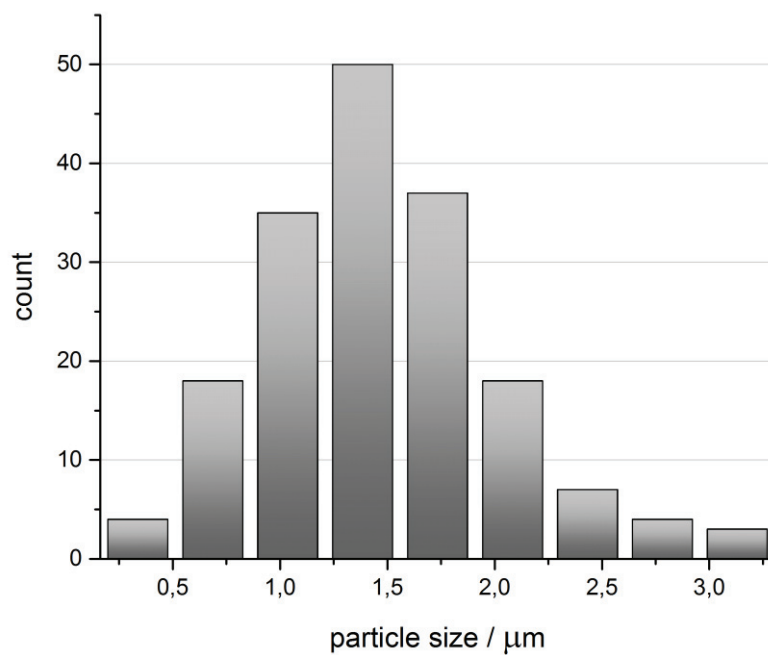


Figure 53: Histogram of the average particle size determined through Figure 52

During the preparation process, one pellet broke into two parts. This fracture point was investigated via SEM. It was possible to find a great concentration of Pr-oxide (Figure 54). This PrO_x contamination might be the possible reason for the fracture.

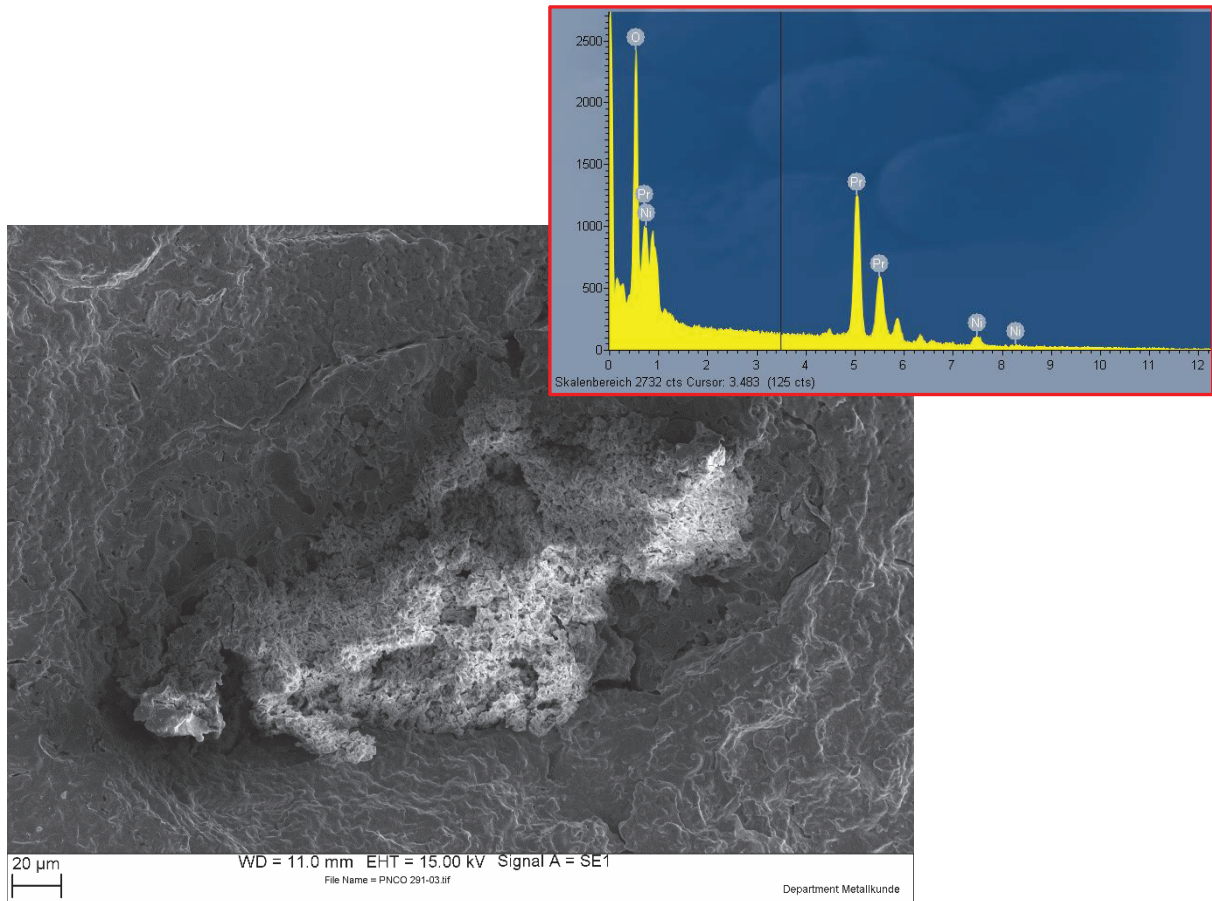


Figure 54: SEM image of a Pr-oxide contamination with EDX image of the composition

4. Summary and Conclusion

The material PNCO was prepared through freeze drying. It was possible to produce single phased powder showing the targeted K_2NiF_4 structure.

The DSC-curve showed a phase decomposition of PNCO. In pure Ar, a transition from the orthorhombic to the tetragonal modification occurs. Thermogravimetry, studied in the temperature range 30-900°C, showed an irreversible mass increase ($T \geq 750^\circ\text{C}$, $p_{O_2} = 0.2$ bar). It confirms the transition to a higher order Ruddlesden Popper phase.

The thermal expansion coefficient (TEC) for PNCO is in average $\alpha = 16 \times 10^{-6} \frac{1}{K}$. This result is slightly higher than TECs of conventional solid electrolytes for instance YSZ ($10 \times 10^{-6} \frac{1}{K}$) and GDO ($13 \times 10^{-6} \frac{1}{K}$) [44].

Subsequently, a dense sample was produced and prepared for measurements in van der Pauw geometry. The sample was contacted and placed in a reactor to perform studies of the oxygen exchange kinetics by the dc-conductivity relaxation method (determination of σ and k_{chem}). With increasing temperature the electrical conductivity σ decreases due to the loss of lattice oxygen. In the range of 600-800°C σ reaches values between 65 and 75 $\frac{S}{cm}$. However, comparing the σ -values of PNCO with those of PNO ($\sigma = 65 - 90 \frac{S}{cm}$), σ decreases significantly. This is attributable to the formation of oxygen vacancies due to substitution with cobalt.

The substitution with Co at the B-site leads to an increase of the materials surface exchange coefficient (in the range of $10^{-4} \frac{cm}{s}$ to $10^{-6} \frac{cm}{s}$) and a decrease in its activation energy ($E_a = \sim 40 \frac{kJ}{mol}$). At low temperatures k_{chem} is approximately an order of magnitude higher than that for PNO ($E_a = \sim 65 \frac{kJ}{mol}$).

All in all, Pr-based K_2NiF_4 -type Ruddlesden Popper materials with the general formula $A_{n+1}B_nO_{3n+1}$ (A=La, Pr, Nd; B=Ni; n=1, 2, 3 ...) are promising oxide materials for future energy technologies. Praseodymium nickelate (PNO) already showed excellent oxygen exchange kinetics. The substitution with Co at the B-site results in a further increase of the oxygen exchange kinetics. However, PNCO's instability (700°C - 1200°C) represents an obstacle to its

practical usage (decomposition into $\text{Pr}_4\text{Ni}_3\text{O}_{10}$ and Pr_6O_{11} phases). The study of higher order Ruddlesden-Popper phases (with $n = 2$ and 3) might offer attractive opportunities for future investigations. These materials also show an increase in electronic conductivity.

References

1. Egger, A., PhD Thesis, Rare earth nickelates as cathodes for solid oxide fuel cells, in Department of General, Analytical and Physical Chemistry. 2013, University of Leoben, Austria. p. 231.
2. Granger, P., et al., eds. Perovskites and related mixed oxides: Concepts and applications, Volume 1. Vol. 1. 2016, Wiley-VCH: Weinheim, Germany. 1056.
3. Ishihara, T., ed. Perovskite oxide for solid oxide fuel cells. Fuel cells and hydrogen energy, ed. N.P. Bansal. 2009, Springer: New York.
4. Stan, C., Alternative Antriebe für Automobile - Hybridsysteme, Brennstoffzellen, alternative Energieträger. Vol. 3. 2005, Berlin Heidelberg Springer Vieweg 399.
5. Zhao, T.S. and N. Meng, eds. Solid oxide fuel cells: From materials to system modeling. 2013, RSC Publishing: Cambridge, UK.
6. Vibhu, V., PhD Thesis, Stability and ageing studies of praseodymium-based nickelates as cathodes for Solid Oxide Fuel Cells. 2016, University of Bordeaux: Bordeaux. p. 239.
7. Allançon, C., et al., Influence of oxygen on structural transitions in $\text{Pr}_2\text{NiO}_{4+\delta}$. Solid State Ionics, 1994. **74**(3-4): p. 239-248.
8. Flura, A., et al., Chemical and structural changes in $\text{Ln}_2\text{NiO}_{4+\delta}$ (Ln=La, Pr or Nd) lanthanide nickelates as a function of oxygen partial pressure at high temperature. Journal of Solid State Chemistry, 2015. **228**: p. 189-198.
9. Vibhu, V., et al., $\text{Pr}_4\text{Ni}_3\text{O}_{10+\delta}$: A new promising oxygen electrode material for solid oxide fuel cells. Journal of Power Sources, 2016. **317**: p. 184-193.
10. Kreuer, K.-D., ed. Fuel Cells - Selected Entries from the Encyclopedia of Sustainability Science and Technology. 1st ed. 2013, Springer-Verlag: New York.
11. Gellings, P.J., The CRC handbook of solid state electrochemistry. 1997, Boca Raton, Fla. [u.a.]: CRC Press.
12. Hayd, J., Nanoskalige Kathoden für den Einsatz in Festelektrolyt-Brennstoffzellen bei abgesenkten Betriebstemperaturen. 2012, PhD Thesis, Universitätsverlag Karlsruhe: Karlsruhe. p. 1-219.
13. van Doorn, R.H.E. and A.J. Burggraaf, Structural aspects of the ionic conductivity of $\text{La}_{1-x}\text{Sr}_x\text{CoO}_{3-\delta}$. Solid State Ionics, 2000. **128**(1-4): p. 65-78.
14. Li, Q., et al., Electrode properties of Co-doped $\text{Ca}_2\text{Fe}_2\text{O}_5$ as new cathode materials for intermediate-temperature SOFCs. International Journal of Hydrogen Energy, 2010. **35**(17): p. 9151-9157.

15. Kilner, J.A., R.A. De Souza, and I.C. Fullarton, Surface exchange of oxygen in mixed conducting perovskite oxides. *Solid State Ionics*, 1996. **86-88**: p. 703-709.
16. Kilner, J.A. and C.K.M. Shaw, Mass transport in $\text{La}_2\text{Ni}_{1-x}\text{Co}_x\text{O}_{4+\delta}$ oxides with the K_2NiF_4 structure. *Solid State Ionics*, 2002. **154-155**: p. 523-527.
17. Boehm, E., et al., Oxygen diffusion and transport properties in non-stoichiometric $\text{Ln}_{2-x}\text{NiO}_{4+\delta}$ oxides. *Solid State Ionics*, 2005. **176**(37-38): p. 2717-2725.
18. Munnings, C.N., et al., Oxygen transport in the $\text{La}_2\text{Ni}_{1-x}\text{Co}_x\text{O}_{4+\delta}$ system. *Solid State Ionics*, 2005. **176**(23-24): p. 1895-1901.
19. Haar, v.d.L.M., PhD Thesis, Mixed-conducting perovskite membranes for oxygen separation. Towards the development of a supported thin-film membrane. 2001, Universiteit Twente: Enschede.
20. Chroneos, A., et al., Oxygen diffusion in solid oxide fuel cell cathode and electrolyte materials: mechanistic insights from atomistic simulations. *Energy & Environmental Science*, 2011. **4**(8): p. 2774-2789.
21. Mehrer, H., Diffusion in solids: fundamentals, methods, materials, diffusion-controlled processes. Vol. 155. 2007, Berlin [etc]: Springer.
22. Chiang, Y.-M., D.P. Birnie, and W.D. Kingery, Physical ceramics: principles for ceramics science and engineering. 1997, New York, NY [u.a.]: Wiley.
23. Sunarso, J., et al., Mixed ionic–electronic conducting (MIEC) ceramic-based membranes for oxygen separation. *Journal of Membrane Science*, 2008. **320**(1-2): p. 13-41.
24. Sullivan, J.D., et al., A conventional and high-resolution synchrotron X-ray diffraction study of phase separations in $\text{Pr}_2\text{NiO}_{4+\delta}$. *Journal of Solid State Chemistry*, 1991. **94**(2): p. 337-351.
25. Abdelwahed, W., et al., Freeze-drying of nanoparticles: Formulation, process and storage considerations. *Advanced Drug Delivery Reviews*, 2006. **58**(15): p. 1688-1713.
26. Christ, Operating Manual Freeze Dryer Alpha 1-2 LDplus. 2005: Martin Christ GmbH.
27. Landstreet, J. Matter and its atomic structure. 2003 [cited 2017; Available from: <http://www.astro.uwo.ca/~jlandstr/planets/webfigs/matter/slide5.html>].
28. Rietveld, G., et al., DC conductivity measurements in the Van Der Pauw geometry. *IEEE Transactions on Instrumentation and Measurement*, 2003. **52**(2): p. 449-453.
29. Bruker-Corporation, XRD User manual - D8 Series. 2017.

30. Speakman, S.A., Basic of X-Ray Powder Diffraction. 2017, Massachusetts Institute of Technology: Center of Material Science and Engineering at MIT.
31. Dinnebier, R.E. and S.J.L. Billinge, Powder Diffraction - Theory and Practice. 2009, Cambridge UK: The Royal Society of Chemistry. 582.
32. Ho, C.Y. and R.E. Taylor, Thermal expansion of solids. 1998: ASM International, Materials Park, OH (United States). Medium: X; Size: 300 p.
33. Netzsch, Dilatometry - Method, Instruments, Applications. 2015. 12.
34. Vyazovkin, S., Thermogravimetric Analysis, in Characterization of Materials. 2002, John Wiley & Sons, Inc.
35. Dean, D., Thermal Gravimetric Analysis. 2012, University of Alabama at Birmingham.
36. Bucher, E., Habilitation Thesis, Defect chemistry and oxygen exchange kinetics of mixed conducting perovskites for solid oxide fuel cell cathodes, in Chair of Physical Chemistry. 2013, Montanuniversität Leoben: Leoben.
37. Höhne, G.W., W. Hemminger, and H.J. Flammersheim, Differential scanning calorimetry - An introduction for practioners. 1996, Berlin Heidelberg: Springer Verlag.
38. Carter, B. The Secret to Perfect Terra Sig - A Ball Mill and a little Crocus Martis 2011; Available from: <http://carterpottery.blogspot.co.at/2011/01/secret-to-perfect-terra-sig-ball-mill.html>.
39. Lutterotti, L., Total pattern fitting for the combined size-strain-stress-texture determination in thin film diffraction. Nuclear Inst. and Methods in Physics Research, 2010. **B(268)**: p. 334-340.
40. Niwa, E., et al., Thermodynamic analyses of structural phase transition of $\text{Pr}_2\text{NiO}_{4+\delta}$ involving variation of oxygen content. Thermochemica Acta, 2014. **575**: p. 129-134.
41. Kharton, V.V., et al., Mixed electronic and ionic conductivity of LaCo(M)O_3 (M=Ga, Cr, Fe or Ni): III. Diffusion of oxygen through $\text{LaCo}_{1-x-y}\text{Fe}_x\text{Ni}_y\text{O}_{3\pm\delta}$ ceramics. Solid State Ionics, 1998. **110(1-2)**: p. 61-68.
42. Kharton, V.V., et al., Characterization of mixed-conducting $\text{La}_2\text{Ni}_{0.9}\text{Co}_{0.1}\text{O}_{4+\delta}$ membranes for dry methane oxidation. Applied Catalysis A: General, 2004. **261(1)**: p. 25-35.
43. Liu, X.Y., Z.H. Xu, and G.Y. Liang, Comparative study of the sintering behaviors between YSZ and LZ/YSZ composite. Materials Letters, 2017. **191**: p. 108-111.

44. Gao, P., et al., Thermal expansion and elastic moduli of electrolyte materials for high and intermediate temperature solid oxide fuel cell. *Solid State Ionics*, 2017. **300**: p. 1-9.
45. Kostogloudis, G.C. and C. Ftikos, Properties of A-site-deficient $\text{La}_{0.6}\text{Sr}_{0.4}\text{Co}_{0.2}\text{Fe}_{0.8}\text{O}_{3-\delta}$ -based perovskite oxides. *Solid State Ionics*, 1999. **126**(1-2): p. 143-151.
46. Bassat, J.M., P. Odier, and J.P. Loup, The Semiconductor-to-Metal Transition in Question in $\text{La}_{2-x}\text{NiO}_{4+\delta}$ ($\delta > 0$ or $\delta < 0$). *Journal of Solid State Chemistry*, 1994. **110**(1): p. 124-135.
47. Amow, G., I.J. Davidson, and S.J. Skinner, A comparative study of the Ruddlesden-Popper series, $\text{La}_{n+1}\text{Ni}_n\text{O}_{3n+1}$ ($n=1, 2$ and 3), for solid-oxide fuel-cell cathode applications. *Solid State Ionics*, 2006. **177**(13): p. 1205-1210.
48. Amow, G. and S.J. Skinner, Recent developments in Ruddlesden–Popper nickelate systems for solid oxide fuel cell cathodes. *Journal of Solid State Electrochemistry*, 2006. **10**(8): p. 538-546.
49. Nomura, T., et al., Electrode properties of doped Pr_2NiO_4 -based oxide cathode for intermediate-temperature SOFCs. *Journal of the Ceramic Society of Japan*, 2012. **120**(1407): p. 534-538.
50. Rahaman, M.N., *Sintering of Ceramics*. 2008, Boca Raton, London, New York: CRC Press. 388.
51. Rahaman, M.N., *Ceramics processing and sintering*. Second Edition ed. 2003, Boca Raton, London, New York: CRC Press. 875.